JAMES | Journal of Advances in Modeling Earth Systems

RESEARCH ARTICLE
10.1029/2024MS004381

# Toward the Direct Simulation of the Quasi-Biennial Oscillation in a Global Storm-Resolving Model

**Henning Franke**[1,2] **and Marco A. Giorgetta**[1]

[1]Max Planck Institute for Meteorology, Hamburg, Germany, [2]International Max Planck Research School on Earth System Modelling, Max Planck Institute for Meteorology, Hamburg, Germany

**Key Points:**

- The ability of the general circulation model ICON, which explicitly simulates deep convection and gravity waves, to simulate a quasi-biennial oscillation (QBO) is tested
- ICON simulates a reasonable downward propagation and momentum balance of QBO-like jets in the upper QBO domain in the first simulation year
- Simulated QBO-like jets stall in lower QBO domain due to a lack of planetary wave forcing due to weak convectively coupled equatorial waves

**Supporting Information:**

Supporting Information may be found in the online version of this article.

**Correspondence to:**

H. Franke,
henning.franke@mpimet.mpg.de

**Citation:**

Franke, H., & Giorgetta, M. A. (2024). Toward the direct simulation of the quasi-biennial oscillation in a global storm-resolving model. *Journal of Advances in Modeling Earth Systems*, *16*, e2024MS004381. https://doi.org/10.1029/2024MS004381

Received 2 APR 2024
Accepted 14 SEP 2024

**Author Contributions:**

**Conceptualization:** Henning Franke, Marco A. Giorgetta
**Formal analysis:** Henning Franke
**Investigation:** Henning Franke, Marco A. Giorgetta
**Methodology:** Henning Franke, Marco A. Giorgetta
**Resources:** Marco A. Giorgetta
**Software:** Henning Franke
**Supervision:** Marco A. Giorgetta
**Visualization:** Henning Franke
**Writing – original draft:** Henning Franke



**Abstract** This study presents the first attempt to simulate a full cycle of the quasi-biennial oscillation (QBO) in a global storm-resolving model (GSRM) that explicitly simulates deep convection and gravity waves instead of parameterizing them. Using the Icosahedral Nonhydrostatic (ICON) model with horizontal and vertical resolutions of about 5 km and 400 m, respectively, we show that an untuned state-of-the-art GSRM is already on the verge of simulating a QBO-like oscillation of the zonal wind in the tropical stratosphere for the right reasons. ICON shows overall good fidelity in simulating the QBO momentum budget and the downward propagation of the QBO jets in the upper QBO domain (25–35 km). In the lowermost stratosphere, however, ICON does not simulate the downward propagation of the QBO jets to the tropopause. This is the result of a pronounced lack of QBO wave forcing, mainly on planetary scales. The lack of planetary-scale wave forcing in the lowermost stratosphere is caused by an underestimation of planetary-scale wave momentum fluxes entering the stratosphere. We attribute this lack of planetary-scale wave momentum fluxes to a substantial lack of convectively coupled equatorial waves (CCEWs) in the tropical troposphere. Therefore, we conclude that in ICON, simulating a realistic spatio-temporal variability of tropical deep convection, in particular CCEWs, is currently the main roadblock toward simulating a reasonable QBO. To overcome this intermediate situation, we propose to aim at an improved explicit simulation of tropical deep convection by retuning the remaining parameterizations of cloud microphysics and vertical diffusion, and by increasing the horizontal resolution.

**Plain Language Summary** The quasi-biennial oscillation (QBO) is a wind system located in the equatorial stratosphere between ~17 and ~35 km and consists of westerly and easterly wind jets that alternately propagate downward with time. The QBO has been shown to influence surface weather, so it is important to simulate the QBO realistically in the computer models typically used for climate research. However, these models often struggle to simulate a realistic QBO because they represent the processes leading up to the QBO, that is, tropical rain showers and short atmospheric waves excited by these rain showers, only empirically through so-called parameterizations. In this study, we attempt for the first time to simulate the QBO in a model that directly represents these processes through an ultra-fine grid. We find that our model maintains QBO-like stratospheric winds throughout the simulation, and in the central stratosphere, the model simulates the characteristics of the QBO reasonably well for the right reasons. However, in the lowermost stratosphere, the simulated QBO is not realistic and does not move downward with time as observed due to a misrepresentation of long waves in the tropical atmosphere. These results will guide future model development to improve the model's representation of the QBO.

## 1. Introduction

The quasi-biennial oscillation (QBO) is a more or less regular downward propagating oscillation of the zonal mean zonal wind in the tropical stratosphere, driven by the breaking and dissipation of upwardly propagating tropical waves (Baldwin et al., 2001). The wave spectrum that drives the QBO ranges from horizontally large-scale planetary waves to small-scale gravity waves (GWs), and the vast majority of these waves are generated by tropical deep convection (e.g., Fritts & Alexander, 2003; Holton, 1972). However, deep convection and a substantial part of the GW spectrum are not resolved by conventional general circulation models (GCMs), which typically employ horizontal grid spacings of $\mathcal{O}(100\,\text{km})$. Therefore, deep convection and GWs are usually parameterized in these models, which leads to considerable uncertainties in the simulated QBO (Bushell et al., 2020). In this study, we present the first attempt to overcome this uncertainty by a direct simulation of a full QBO cycle in a GCM that no longer parameterizes deep convection and GWs but instead explicitly simulates both processes—and thus the entire QBO forcing.

**Writing – review & editing:**
Henning Franke, Marco A. Giorgetta

Successfully modeling the QBO in a realistic manner has ever since posed a major challenge to conventional three-dimensional GCMs, and the fidelity of simulated QBOs in such models has increased only slightly over the last two decades (Richter, Anstey, et al., 2020; Schenzinger et al., 2017). This motivated the recent model intercomparison project Quasi-Biennial Oscillation initiative (QBOi), which aimed to assess the status quo of the ability of the latest GCMs to simulate a QBO and to identify possible avenues for improvement (Butchart et al., 2018). As one of the main results of QBOi, it was shown that the partitioning of the QBO wave forcing between resolved and parameterized waves is highly model-dependent, with the contribution of the parameterized GWs varying between 40% and 80% (Bushell et al., 2020). On the one hand, this large intermodel spread can be directly attributed to the inherent uncertainty of the GW parameterizations themselves, which results from the necessary simplifying assumptions in their formulation. These simplifications include that most GW parameterizations allow only for instantaneous and vertical GW propagation, often do not account for GW intermittency and secondary generation, and usually prescribe a fixed GW source spectrum (Achatz et al., 2023; Plougonven et al., 2020). The prescribed GW source spectrum is still poorly constrained by observations and thus varies widely between different models (Alexander et al., 2010). On the other hand, the uncertainty in the relative contribution of resolved and parameterized waves to driving the QBO is a consequence of the fact that GW parameterizations are often used to optimize the simulated QBO to achieve a somewhat realistic QBO period and amplitude (e.g., Garfinkel et al., 2022).

In part, the tuning becomes necessary to compensate for biases in the resolved wave forcing of the QBO. These biases often arise from the parameterization of deep convection, which affects the representation of convectively coupled equatorial waves (CCEWs) (e.g., Frierson et al., 2011; Lin et al., 2008; Straub et al., 2010). Since CCEWs are closely related to stratospheric equatorial waves (SEWs), the details of the parameterization of deep convection can affect the resolved wave momentum fluxes in the lower stratosphere, which contribute to driving the QBO (Horinouchi et al., 2003; Ricciardulli & Garcia, 2000). Furthermore, the parameterization of deep convection directly or indirectly provides the input fields that are used to estimate the wave sources of interactive GW parameterizations (e.g., Beres et al., 2004; Bushell et al., 2015; Richter et al., 2010), thereby influencing the parameterized GW forcing of the QBO.

Obviously, the uncertainties associated with the parameterizations of deep convection and GWs lead to substantial uncertainty in the overall QBO momentum budget. This severely limits our current understanding of the details of the QBO forcing. Moreover, the GW parameterizations in many GCMs are overtuned toward a realistic representation of the present-day QBO, which prevents insight into out-of-sample conditions, as demonstrated for the question of how the QBO may change due to global warming (Richter, Butchart, et al., 2020; Schirber et al., 2015). Despite recent progress in the development of more sophisticated GW parameterizations (e.g., Bölöni et al., 2021; Y.-H. Kim et al., 2021), it is questionable whether the current approach to modeling the QBO will allow for fundamental new insights in the foreseeable future.

As a starting point to overcome this parameterization deadlock, Giorgetta et al. (2022) presented the first direct simulation of QBO jets over a short period of 48 days in a very high resolution GCM (~5 km horizontal, ~400 m vertical) that no longer employs a parameterization of deep convection and GWs. This type of GCMs is commonly referred to as global storm-resolving models (GSRMs) (e.g., Satoh et al., 2019; Stevens et al., 2019). GSRMs offer substantial potential for reducing the long-standing uncertainty in modeling the QBO. However, current GSRMs mostly employ horizontal grid spacings between $\mathcal{O}$(1 km) and $\mathcal{O}$(10 km). These grid spacings are often referred to as the "convective gray zone" because they partially but not fully resolve deep convection, and thus neither traditional parameterizations of deep convection nor its explicit treatment work satisfactorily (e.g., Prein et al., 2015; Tomassini et al., 2023). As shown by Polichtchouk et al. (2021), these problems in representing deep convection also affect the details of the simulated tropical GW spectrum, that is, the partitioning of the resolved GW momentum flux (GWMF) with respect to horizontal wavelength. They suggest that even at a horizontal grid spacing of less than 5 km, a scale-aware parameterization of deep convection may be necessary to accurately simulate the resolved GWMF.

However, it is currently unclear whether this fidelity in representing the details of the GW spectrum is really necessary for the simulation of a realistic QBO, or whether major aspects of the QBO can be already well captured in a GSRM operating in the gray zone. This question cannot be answered by the short simulation of Giorgetta et al. (2022), although they have shown that a state-of-the-art GSRM is in principle capable of simulating a reasonable wave-driven downward propagation of the QBO jets over a period of 48 days. Such short simulations

can only work as a first proof of concept and allow for specific process studies, as demonstrated by Franke et al. (2023), who showed that the QBO is likely to become faster and stronger under global warming based on warming-induced changes of the QBO GW forcing. However, such short studies do not allow for a systematic evaluation of the QBO and its forcing, which requires the simulation of at least one full QBO cycle.

This situation motivates the present study, which aims at the first direct simulation of a full QBO cycle in a GSRM which neither applies a parameterization of deep convection nor GWs. The simulation was performed by the global storm-resolving Icosahedral Nonhydrostatic (ICON) model with a horizontal grid spacing of about 5 km and a vertical grid spacing between 350 m and 560 m in the stratosphere. As this is the first simulation of its kind over such a long period, we certainly do not expect the model to simulate a QBO that is already close to reality. Rather, we want to find out whether a GSRM in the chosen configuration is able to capture the basic characteristics and dynamics of the QBO and which aspects need further improvement. In doing so, we aim to provide a benchmark simulation to guide future model development. More specifically, we will address the following research questions:

1. *Is the state-of-the-art GSRM ICON in the present configuration capable of directly simulating a full cycle of the QBO in a reasonable way? Which aspects of the QBO are well captured and which are not?*
2. *Why does the model simulate the QBO the way it does?*
3. *If the QBO is reasonably simulated, how is it forced in the simulation? Is it reasonable for the right reasons, or is it the product of compensating errors?*
4. *If the QBO is not reasonably simulated, what are the sources of QBO biases? Are QBO biases caused by biases in other aspects of the simulation?*

## 2. Methods

### 2.1. Global Storm-Resolving ICON Simulation

We conducted a two-year-long global storm-resolving simulation with the non-hydrostatic GSRM ICON in an atmosphere-only setup (Giorgetta et al., 2018). Following the scientific rationale of our study, this simulation employs neither a parameterization of deep convection nor a parameterization of orographic and non-orographic GWs. Instead, the horizontal and vertical resolution allows for an explicit representation of these processes. Horizontally, the simulation uses the R2B9 grid, which has an equivalent grid spacing of ∼4.9 km (see Giorgetta et al., 2018, Table 1), and vertically it uses a grid with 191 levels up to an altitude of 83 km, resulting in a vertical grid spacing of ∼350 m in the tropopause region and ∼560 m in the stratopause region (see Giorgetta et al., 2022, Figure 1). To ensure the numerical stability of the model, we performed the simulation with a timestep of 30 s, which was further divided into eight dynamics substeps. In contrast, Giorgetta et al. (2022) used a timestep of 40 s and five dynamics substeps, which proved to be not stable enough for longer simulations. Details on the dynamical substepping can be found in Zängl et al. (2015). Since this storm-resolving model setup is computationally very demanding, we performed the simulation with the graphics processing unit (GPU)-enabled version of ICON (Giorgetta et al., 2022).

The storm-resolving configuration of ICON retains parameterizations for only three remaining processes: radiation, cloud microphysics, and turbulent vertical diffusion. For radiation, the GPU-enabled ICON employs the RTE + RRTMGP scheme (Pincus et al., 2019). Cloud microphysics is parameterized using a one-moment "graupel" microphysics scheme (Baldauf et al., 2011; Doms et al., 2021). The vertical diffusion of heat, momentum, and tracers is parameterized using a total turbulent energy scheme (Mauritsen et al., 2007; Pithan et al., 2015). This scheme represents the size of the largest turbulent eddies by calculating a turbulent length scale $l$, which by default is capped at $l_{max} = 150$ m outside the boundary layer (Pithan et al., 2015). In our simulation, we reduced $l_{max}$ to 50 m because $l_{max} = 150$ m was found to lead to unreasonably strong vertical diffusion. For details on the parameterizations, please refer to Giorgetta et al. (2018, 2022).

In ICON, explicit horizontal diffusion is employed as a second-order Smagorinsky diffusion acting on potential temperature and horizontal velocity combined with a fourth-order background diffusion acting on horizontal velocity only with an $e$-folding time of 1,080 s. In addition, ICON employs a fourth-order divergence damping acting on three-dimensional divergence in order to ensure numerical stability. To avoid the unphysical reflection of waves at the top of the model, ICON employs a Rayleigh damping acting on the vertical velocity above 50 km

(Klemp et al., 2008). Details on the formulation of the diffusion and damping acting in ICON can be found in Zängl et al. (2015).

The simulation itself was set up as a 2-year-long time slice experiment initialized from the operational analysis of the Integrated Forecasting System of the European Centre for Medium-Range Weather Forecasts (ECMWF) on 1 April 2004 at 00:00:00 UTC. The boundary conditions closely follow the experimental protocol of the QBOi Experiment 2 (Butchart et al., 2018). Accordingly, the sea surface temperature and the sea ice concentration have been prescribed as a repeating annual cycle of the 1988–2007 monthly means from the corresponding Coupled Model Intercomparison Project Phase 6 (CMIP6) input data sets (Durack & Taylor, 2019). The concentrations of carbon dioxide ($CO_2$) and other radiatively active trace gases except ozone ($O_3$) were also set to their 1988–2007 mean values from the CMIP6 input data set (Meinshausen et al., 2017), resulting in a concentration of 365.59 ppm. The $O_3$ concentration is modeled interactively using the linearized ozone scheme of Cariolle and Teyssèdre (2007). Tropospheric aerosols are prescribed with their 2002 monthly means from the Max Planck Institute aerosol climatology (MAC; Kinne et al., 2013), and the solar forcing is also prescribed with its 2002 monthly means. The year 2002 was chosen based on the QBOi experimental protocol (Butchart et al., 2018).

The simulation is analyzed based on three-hourly instantaneous output of atmospheric state variables and three-hourly averaged output of tendencies and fluxes. The output has been interpolated from the native triangular R2B9 grid to a regular n256 Gaussian grid, which has a grid spacing of ∼39 km at the equator, using a distance-weighted remapping of the 13 nearest neighbors. The three-dimensional output fields were then further interpolated vertically from the native terrain-following hybrid sigma height coordinate to geometric height levels corresponding to the sigma height levels over ocean. Since the transition from terrain-following coordinate surfaces to flat coordinate surfaces occurs at an altitude of 22.5 km, the target height levels of the vertical interpolation are identical to the model levels above this altitude.

### 2.2. Reference Data Sets

To evaluate the simulated QBO, its zonal momentum budget, and the equatorial wavefield, we compare the simulation to observationally constrained reference data sets.

#### 2.2.1. ERA5 Reanalysis

As a reference for the QBO and its zonal momentum budget, we use the ECMWF Reanalysis v5 (ERA5; Hersbach et al., 2020). We use only one reanalysis data set as a reference because the representation of the QBO is very similar in different recent state-of-the-art reanalyzes (SPARC, 2022, Chapter 9). The representation of the QBO in ERA5 itself has been investigated in detail by Pahlavan, Fu, et al. (2021) and Pahlavan, Wallace, et al. (2021).

ERA5 has a spectral truncation of T639, corresponding to an n320 Gaussian grid, which has a grid spacing of ∼31 km, and 137 hybrid sigma pressure levels up to 0.01 hPa. The three wind components, temperature, and the surface geopotential are provided on the original T639 spectral grid, while tracer and two-dimensional surface fields are provided on a reduced n320 Gaussian grid (Hersbach et al., 2018a, 2018b). Thus, in a first step, we interpolated the raw ERA5 data to the same regular n256 Gaussian grid as the ICON output using a distance-weighted remapping of the four nearest neighbors. We then interpolate the ERA5 data to the 191 geometric height levels of the postprocessed ICON output.

Please note that we used ERA5.1 instead of ERA5 for the period 2000–2006. This is due to the fact that ERA5 has a pronounced stratospheric cold bias during these years due to incorrect data assimilation, which has been fixed in ERA5.1 (Simmons et al., 2020). When we refer to ERA5 throughout this manuscript, we implicitly mean ERA5.1 during the years 2000–2006.

#### 2.2.2. IMERG Precipitation Observations

As an additional reference data set for tropical precipitation, we use a satellite-based observational product, the Integrated Multi-satellite Retrievals for the Global Precipitation Measurement (IMERG) for the period 1 April 2004–31 March 2006 (Huffman et al., 2022). IMERG provides the half-hourly mean precipitation rate with a spatial resolution of $0.1° \times 0.1°$. We resampled the data to three-hourly mean precipitation rates to match the temporal resolution of the ICON output. Afterward, we interpolated the data to the same regular n256 Gaussian grid as the ICON output, using a distance-weighted average remapping of the four nearest neighbors.

### 2.3. Diagnostics

#### 2.3.1. Equatorial Wave Spectra

We investigate the equatorial wavefield by means of spectral analysis in longitude $\lambda$ and time $t$. The two-dimensional power spectrum $P_x$ of a quantity $x(\lambda, t)$ with respect to zonal wavenumber $k$ and frequency $\omega$ is calculated as

$$P_x(k, \omega) = \frac{1}{N_\lambda^2 N_t^2} \mathcal{F}_x(k, \omega)\tilde{\mathcal{F}}_x(k, \omega), \tag{1}$$

where $N_\lambda$ denotes the number of grid points in longitude, $N_t$ denotes the number of samples in time, and $\mathcal{F}_x(k, \omega)$ is the complex Fourier transform of $x(\lambda, t)$:

$$\mathcal{F}_x(k,\omega) = \sum_{\lambda=0}^{N_\lambda-1} \sum_{t=0}^{N_t-1} x(\lambda, t)\, e^{-2\pi i \frac{\lambda k}{N_\lambda}}\, e^{-2\pi i \frac{t\omega}{N_t}}. \tag{2}$$

$\tilde{\mathcal{F}}_x$ is the complex conjugate of $\mathcal{F}_x$. The chosen normalization of $P_x(k, \omega)$ satisfies Parseval's theorem as

$$\frac{1}{N_\lambda N_t} \sum_{i=1}^{N_\lambda} \sum_{j=1}^{N_t} \left|x_{i,j}^2\right| = \sum_{k=-N_\lambda/2}^{N_\lambda/2} \sum_{\omega=-N_t/2}^{N_t/2} P_x(k, \omega). \tag{3}$$

Analogously, we define the cospectrum of two quantities $x(\lambda, t)$ and $y(\lambda, t)$ as

$$P_{xy}(k, \omega) = \frac{1}{N_\lambda^2 N_t^2} \Re\left(\mathcal{F}_x(k, \omega)\tilde{\mathcal{F}}_y(k, \omega)\right), \tag{4}$$

where $\Re$ denotes the real part.

To diagnose CCEWs, we follow the methodology of Wheeler and Kiladis (1999) and split a quantity $x(\lambda, \phi, t)$, which depends on latitude $\phi$ into its symmetric and antisymmetric component with respect to the equator, $x_{sym}(\lambda, \phi, t)$ and $x_{asym}(\lambda, \phi, t)$, respectively:

$$\begin{aligned} x_{sym}(\lambda, \phi, t) &= \frac{x(\lambda, \phi, t) + x(\lambda, -\phi, t)}{2} \\ x_{asym}(\lambda, \phi, t) &= \frac{x(\lambda, \phi, t) - x(\lambda, -\phi, t)}{2}. \end{aligned} \tag{5}$$

We then compute the zonal wavenumber-frequency spectra of $x_{sym}(\lambda, \phi, t)$ and $x_{asym}(\lambda, \phi, t)$ as described in Equation 1 and normalize them by a smoothed background spectrum.

#### 2.3.2. QBO Momentum Budget

To understand what processes drive the QBO in the ICON simulation, we diagnose the QBO zonal momentum budget in the transformed Eulerian mean (TEM) framework (Andrews & McIntyre, 1976). The TEM framework allows for a clear separation between the different forcing processes of the QBO. We calculate the TEM zonal momentum budget based on the hydrostatic primitive equations in geometric height coordinates (Hardiman et al., 2010):

$$\overline{u}_{,t} = \overline{v}^* \left(f - \frac{(\overline{u}\cos\phi)_{,\phi}}{a\cos\phi}\right) - \overline{w}^* \overline{u}_{,z} + \frac{\nabla \cdot \boldsymbol{F}}{\overline{\rho} a \cos\phi} + \overline{X}. \tag{6}$$

Here, $u$ denotes the zonal wind, $f$ denotes the Coriolis parameter, $\rho$ denotes the air density, $a$ denotes Earth's mean radius, which we set to $a = 6371$ km, $\phi$ denotes the latitude, $v^*$ and $w^*$ denote the meridional and vertical residual velocity, respectively, and $\boldsymbol{F}$ denotes the Eliassen-Palm (EP) flux. Furthermore, an overbar represents the zonal

mean, and the subscripts $(,t)$, $(,\phi)$, and $(,z)$ denote the partial derivatives with respect to time, latitude, and altitude, respectively.

In Equation 6, the first and second term on the right-hand-side represent the acceleration of $\overline{u}$ by the meridional and vertical residual advection of zonal mean axial angular momentum per unit mass, respectively. The third term on the right-hand-side of Equation 6 represents the wave forcing of $\overline{u}$ which is resolved by the analysis grid, and $\nabla \cdot \boldsymbol{F}$ is given by

$$\nabla \cdot \boldsymbol{F} = \frac{\left(\cos\phi F^{(\phi)}\right)_{,\phi}}{a\cos\phi} + F^{(z)}_{,z}, \tag{7}$$

where $F^{(\phi)}$ and $F^{(z)}$ denote the meridional and vertical component of $\boldsymbol{F}$, respectively. They are given by

$$\begin{aligned} F^{(\phi)} &\equiv -a\cos\phi\ \overline{(\rho v)'u'} + \psi\overline{u}_{,z} \\ F^{(z)} &\equiv -a\cos\phi\ \overline{(\rho w)'u'} - \psi\left(\frac{(\overline{u}\cos\phi)_{,\phi}}{a\cos\phi} - f\right). \end{aligned} \tag{8}$$

Here, a prime represents the deviation from the zonal mean, and $\psi$ denotes the "difference stream function" (cf., Hardiman et al., 2010) and is defined as

$$\psi \equiv \frac{a\cos\phi}{\left|\nabla\overline{\theta}\right|^2}\left(\overline{(\rho v)'\theta'}\ \overline{\theta}_{,z} - \overline{(\rho w)'\theta'}\ \frac{\overline{\theta}_{,\phi}}{a}\right), \tag{9}$$

where $\theta$ denotes the potential temperature. The fourth term on the right-hand-side of Equation 6, $\overline{X}$, represents the residuum which remains when subtracting the previous three terms from the actual zonal wind tendency simulated by ICON. This means that $\overline{X}$ contains all tendencies from processes not resolved by the TEM analysis, including the parameterized tendency from vertical diffusion and diffusive tendencies from the dynamical core itself.

Following Horinouchi et al. (2003), we also calculate spectra of $\boldsymbol{F}$ as a function of zonal wavenumber $k$ and frequency $\omega$:

$$\begin{aligned} F^{(\phi)}(k,\omega) &\equiv -a\cos\phi\ P_{(\rho v)'u'}(k,\omega) + \psi(k,\omega)\,\overline{u}_{,z} \\ F^{(z)}(k,\omega) &\equiv -a\cos\phi\ P_{(\rho w)'u'}(k,\omega) - \psi(k,\omega)\left(\frac{(\overline{u}\cos\phi)_{,\phi}}{a\cos\phi} - f\right) \end{aligned} \tag{10}$$

with

$$\psi(k,\omega) \equiv \frac{a\cos\phi}{\left|\nabla\overline{\theta}\right|^2}\left(P_{(\rho v)'\theta'}(k,\omega)\,\overline{\theta}_{,z} - P_{(\rho w)'\theta'}(k,\omega)\ \frac{\overline{\theta}_{,\phi}}{a}\right). \tag{11}$$

Here, the cospectra $P_{(\rho v)'u'}$ and $P_{(\rho w)'u'}$ as well as $P_{(\rho v)'\theta'}$ and $P_{(\rho w)'\theta'}$ are calculated based on Equation 4. For both ICON and ECMWF Reanalysis v5 (ERA5), we compute the TEM diagnostics based on the postprocessed data on the n256 Gaussian grid with 191 geometric height levels. This procedure follows the recommendations of Hardiman et al. (2010) for comparing TEM diagnostics between data sets on different native grids. It should be noted that the vertical remapping of the ERA5 data prior to the calculation of the TEM diagnostics can result in artifacts in the calculates wave forcing. However, we found this effect to be negligible.

## 3. General Structure of the QBO-Like Oscillation in the ICON Simulation

Figure 1a shows the time evolution of the stratospheric 5° S–5° N mean zonal wind in the ICON simulation. Throughout the entire simulation, ICON sustains a QBO-like zonal wind structure of easterly and westerly wind jets alternating with altitude. The easterly shear zone (i.e., a change of winds from westerly to easterly with

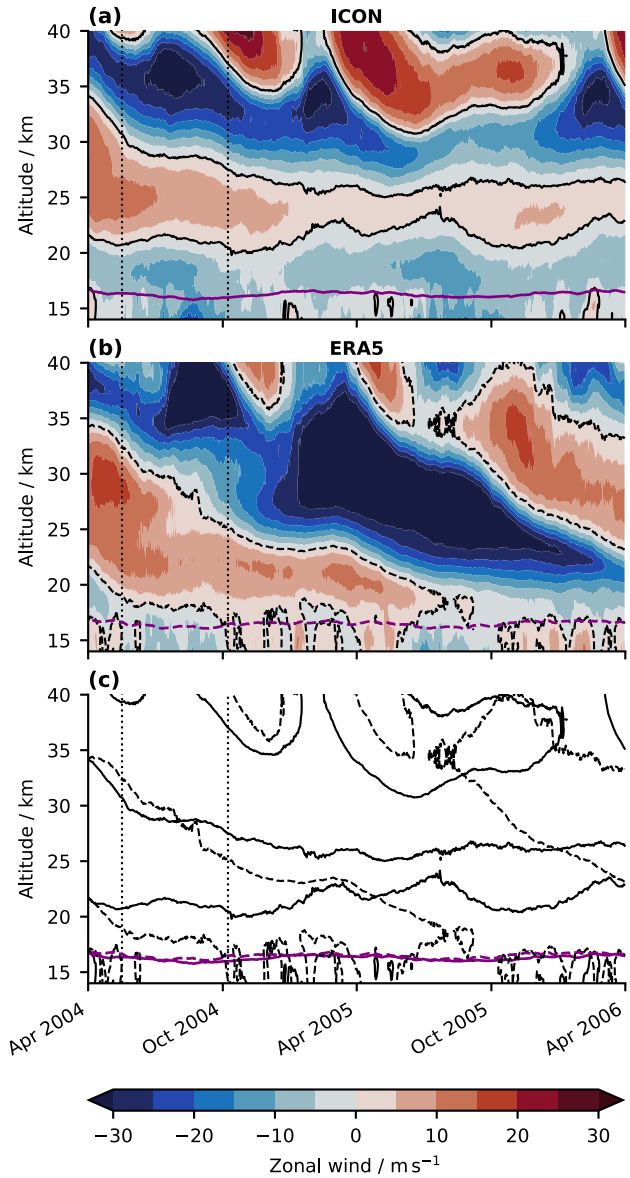


**Figure 1.** Time-altitude cross section of the 5° S–5° N mean zonal wind for (a) the ICON simulation and (b) the ERA5 reanalysis during 1 April 2004–31 March 2006. The (a) solid and (b) dashed black contour lines mark the 0 m $s^{-1}$-isotach. The (a) solid and (b) dashed purple contour lines mark the 370*K*-isentrope, which serves as a proxy for the tropopause altitude. Panel (c) shows the 0 m $s^{-1}$-isotachs and 370*K*-isentropes of panels (a and b) to allow a direct comparison between ICON and ERA5. The vertical dotted black lines in all panels mark the beginning and end of the period used to compare the zonal momentum budgets of the 5° S–5° N mean zonal wind in ICON and ERA5 (see Section 4.2).

altitude), which is initially located between ∼30 and ∼38 km, shows a clear downward propagation during the first year of the simulation. However, the downward propagation of the easterly shear zone stops in the second year of the simulation, and the westerly shear zone, which is initially located between 18 and 25 km, does not propagate downward at all. As a result, the westerly jet stalls and does not dissipate within the simulated period of 2 years, which means that ICON does not simulate a closed cycle of the QBO. Nevertheless, from now on we will refer to the spatio-temporal structure of the zonal wind in the equatorial stratosphere in the ICON simulation—as seen in Figure 1a—as the ICON-QBO.

In the following, we compare the ICON-QBO with selected individual QBO cycles in the ERA5 reanalysis during the years 1980–2015. This period has boundary conditions reasonably close to those of the ICON simulation, and it is free of QBO disruptions such as those observed in 2015/16 and 2019/20 (see Anstey et al., 2021; Osprey et al., 2016). To select reasonable individual QBO cycles for comparison, we first determine those years in which the QBO in March and April was in a phase comparable to that of March and April 2004 because we initialized the ICON simulation on 1 April 2004. The applied criterion for this subsampling is a change of the monthly mean 5° S–5° N mean zonal wind at one of the four levels between 21 and 22.5 km (i.e., 22.432 km, 22.051 km, 21.672 km, 21.296 km) from easterly in March to westerly in April. This criterion is fulfilled by 6 years (1985, 1990, 1997, 2004, 2008, and 2013), which we will hereafter refer to as the ERA5-QBO-ensemble.

In Figure 2, we compare the time evolution of the 5° S–5° N mean zonal wind between the ICON simulation and the ERA5-QBO-ensemble. The basic spatio-temporal structure of the ICON-QBO is approximately within the cycle-to-cycle variability of the ERA5-QBO-ensemble in the first year of the simulation (Figure 2a). During this period, ICON simulates an overall reasonable downward propagation of that 0 m $s^{-1}$-isotach, which is initially located at ∼34 km, at a rate comparable to that of individual cycles in the ERA5-QBO-ensemble. This also applies to the zonal wind jets associated with the semiannual oscillation (SAO) between 35 and 40 km. In the lowermost stratosphere, the comparison between the ICON-QBO and the ERA5-QBO-ensemble reveals the unrealistic lack of downward propagation of the westerly jet of the ICON-QBO right from the beginning of the simulation, which was already identified in Figure 1a. During the second year of the simulation, the spatio-temporal structure of the ICON-QBO is no longer consistent with the ERA5-QBO-ensemble throughout the entire stratosphere.

Figure 2b further shows that the jets of the ICON-QBO are weaker than those of the ERA5-QBO-ensemble in both the lower and upper QBO domain throughout the entire simulation. The vertical structure of ICON-QBO is not consistent with the ERA5-QBO-ensemble right from the beginning of the simulation. In addition, Figure 2b clearly shows that the ICON-QBO is trapped at the end of the simulation due to its lack of downward propagation.

Although the six individual QBO cycles of the ERA5-QBO-ensemble do not provide a statistically significant reference sample, we conclude at this point that the ICON-QBO is not realistic. It suffers from a pronounced lack of downward propagation, which begins in the lowermost stratosphere right at the beginning of the simulation and appears to spread upward subsequently. During the last months of the simulation, basically all zonal wind jets of the ICON-QBO below ∼30 km do no longer propagate downward.

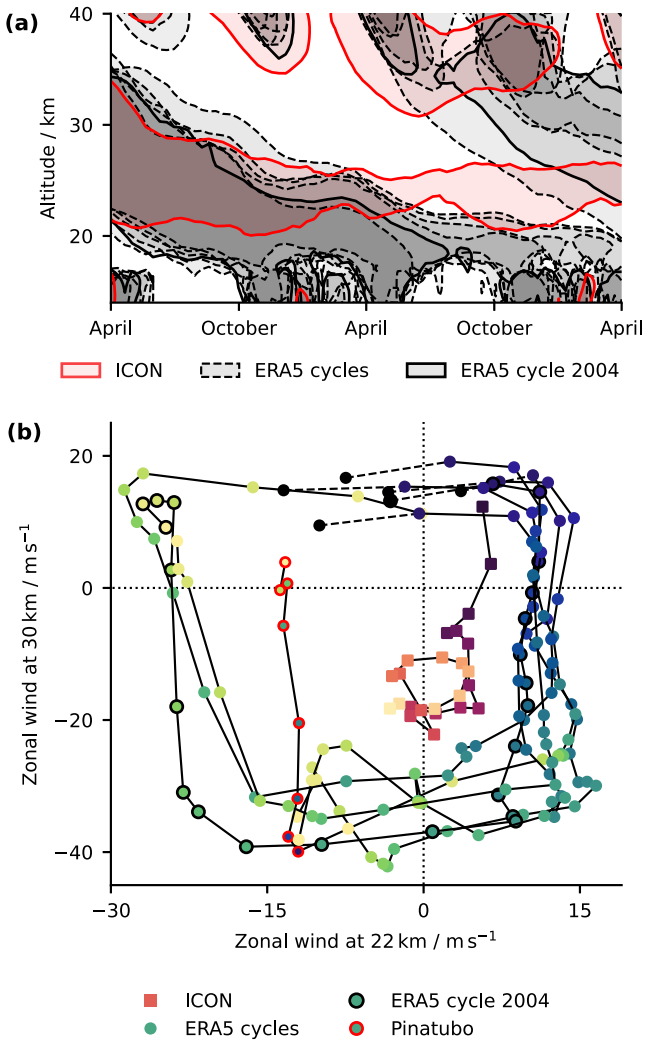


**Figure 2.** (a) Time-altitude cross section of the 5° S–5° N daily mean zonal wind of the ICON simulation and the six individual QBO cycles of the ERA5-QBO-ensemble, starting on April 1 of the years 1985, 1990, 1997, 2004, 2008, and 2013. The shading highlights westerlies, and the contour lines mark the 0 m $s^{-1}$-isotach, with the ERA5 QBO cycle starting on 1 April 2004 being highlighted by a solid black contour. (b) Temporal trajectory of pairs of 5° S–5° N monthly mean zonal wind at ∼22 and ∼30 km for the ICON simulation and the six individual QBO cycles of the ERA5-QBO-ensemble, starting in April of the years 1985, 1990, 1997, 2004, 2008, and 2013. The trajectories start at the dark points, and for the ERA5-QBO-ensemble, the very first dark point, which is connected by a dashed line, marks the wind pair of March prior the "official" two-year-period starts. In the ERA5 QBO cycle starting on 1 April 1990, months after the eruption of Mt. Pinatubo in June 1991 are highlighted by red circles.

To further highlight the shortcomings of the ICON-QBO in more detail, we compare it to one specific QBO cycle of the ERA5-QBO-ensemble, which is the cycle beginning on 1 April 2004 (Figure 1b). The comparison with a single QBO cycle is justified because all individual QBO cycles of the ERA5-QBO-ensemble agree reasonably well among each other, except for the cycle affected by the eruption of Mt. Pinatubo (Figure 2b). From now on, we will refer to the ERA5 QBO cycle beginning on 1 April 2004 as the ERA5-QBO. The comparison between the ICON-QBO and the ERA5-QBO basically confirms the previous results, and in particular highlights that the ICON-QBO has too weak jets below 30 km, especially during the second year of the simulation. During this period, the jets of the ICON-QBO also have a much smaller vertical extent than those of the ERA5-QBO. In addition, the vertical gradient of the zonal wind within the shear zones of the ICON-QBO is much weaker than in those of the ERA5-QBO, at least below 30 km.

Figure 1 also shows that the altitude of the tropopause in the ICON simulation and the ERA5 reanalysis is approximately identical. Thus, we already rule out a too high tropopause in ICON as a root cause for the lack of downward propagation of the ICON-QBO in the lowermost stratosphere. Instead, the downward propagation of the ICON-QBO stops well above the tropopause, while the ERA5-QBO propagates down to the tropopause.

## 4. The Momentum Budget of the ICON-QBO in the TEM Framework

To understand why the ICON-QBO shows the pronounced lack of downward propagation as identified in Section 3, we evaluate its zonal momentum budget in the TEM framework calculated as described in Section 2.3.2.

### 4.1. Spatio-Temporal Structure of the TEM Forcing in the Equatorial Stratosphere in the ICON Simulation

Figure 3 shows the time-altitude cross sections of the stratospheric 5° S–5° N mean zonal wind tendencies in the TEM framework. In general, the spatio-temporal structure of the various TEM tendencies corresponds well to the standard QBO paradigm. The zonal wind tendency due to the vertical EP flux divergence is centered in the shear zones of the ICON-QBO and acts to drive their downward propagation (Figure 3c). In contrast, the zonal wind tendency due to vertical residual advection acts against the downward propagation of the QBO shear zones, especially that of the easterly shear zone, which is initially located between 30 and 38 km (Figure 3a). The zonal wind tendency due to meridional advection is negligibly small in the shear zones of the ICON-QBO and is only relevant for the dynamics of the SAO (Figure 3b). The zonal wind tendency due to the meridional EP flux divergence is strongest in the shear zones above ∼25 km (Figure 3d), where it facilitates the downward propagation of the zonal wind jets, in particular those of the SAO. Below 25 km, the zonal wind tendency due to meridional EP flux divergence is small overall. All of these findings highlight that the basic dynamics of the QBO are well captured by the global storm-resolving ICON simulation.

However, the sum of all TEM tendencies does not match the total zonal wind tendency of the ICON simulation (Figure 3h) Consequently, the TEM zonal momentum budget of the ICON-QBO is closed by a large residuum (Figure 3e). Figure 3 shows that the residuum strongly counteracts the zonal wind tendency due to vertical EP flux divergence. This strong cancellation between the vertical EP flux divergence and the residuum is very similar to the findings of Yao and Jablonowski (2013, 2015). They argue that the strong residuum of the TEM momentum budget is due to the direct effect of implicit and explicit diffusion on the QBO jets. This attribution is questionable

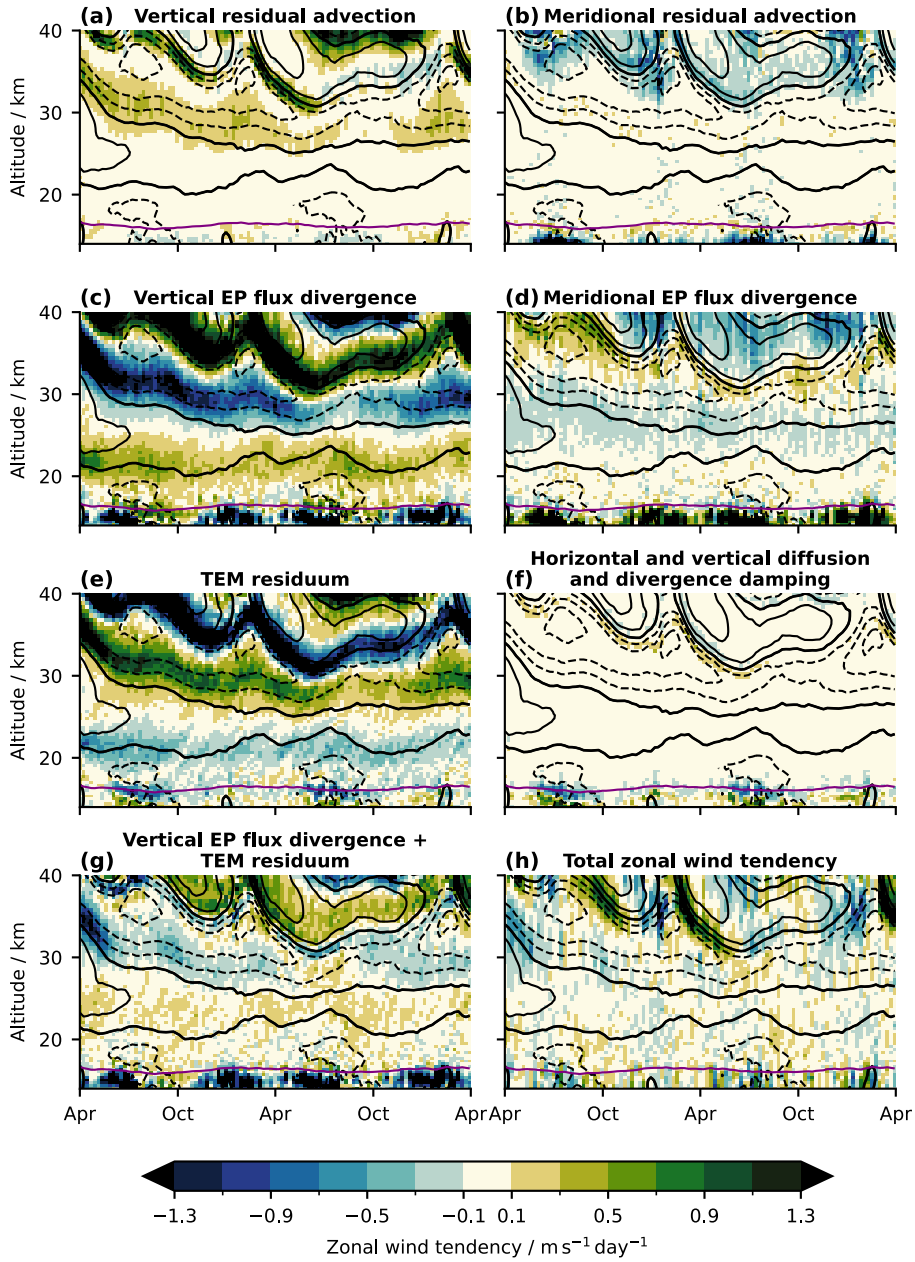


**Figure 3.** Time-altitude cross section of the 5° S–5° N mean weekly-averaged transformed Eulerian mean (TEM) zonal wind tendencies in the ICON simulation starting on 1 April 2004: (a and b) zonal wind tendency due to vertical and meridional residual advection, respectively, (c and d) zonal wind tendency due to vertical and meridional EP flux divergence, respectively, (e) TEM residuum, (f) zonal wind tendency due to horizontal and vertical diffusion and divergence damping, (g) sum of the zonal wind tendency due to vertical EP flux divergence and the TEM residuum, and (h) the total zonal wind tendency. Black contour lines show isotachs of the 5° S–5° N mean zonal wind in intervals of 10 m $s^{-1}$ with negative values being dashed, positive values being solid, and the 0 m $s^{-1}$-isotach being bold solid. Purple contours mark the 370 K-isentrope, which is a proxy for the tropopause altitude.

for the ICON simulation, since the zonal wind tendency due to explicit diffusive processes (i.e., horizontal diffusion, divergence damping, parameterized vertical diffusion) in the equatorial stratosphere is negligibly small throughout the entire simulation, except for the tropopause region and the shear zones below the SAO jets, and clearly cannot explain the TEM residuum (Figure 3f). Apparently, explicit diffusive processes do not directly

damp the jets of the ICON-QBO. Therefore, we conclude that too strong explicit diffusive processes are not the root cause of the lack of downward propagation of the ICON-QBO in the sense that they directly damp the QBO.

Based on the results of Yao and Jablonowski (2013, 2015), the negligible contribution of explicit diffusive processes to the TEM residuum would suggest that the TEM residuum is mainly the imprint of implicit diffusion of ICON's dynamical core. Furthermore, we speculate that the TEM residuum in the ICON simulation may have non-physical causes. Detailed analysis has provided some evidence that the ICON simulation suffers from numerical noise, which appears as systematic features in the simulated atmospheric flow, including the horizontal and vertical wind components. Therefore, the noise is sampled by the instantaneous TEM diagnostics, which diagnose these flow features as a physical signal. This could ultimately lead to an overestimation of the vertical component of the EP flux and its divergence. However, if the noise is generated in-situ at individual model levels and does not propagate upward, the divergence of the overestimated vertical EP flux would be purely diagnostic and would not correspond to wave-mean flow interactions of a vertically propagating wave, which accelerates the mean flow. In that case, the TEM momentum budget must be closed by a huge residuum. In contrast, the impact of the horizontal remapping of the model output from ICON's native grid to the n256 Gaussian analysis grid on the TEM residuum is relatively small (see Supporting Information S1). Ultimately, the exact root cause of the TEM residuum in the ICON simulation is still unclear and its more detailed analysis is a clear target for future research.

Given the strong cancellation between the zonal wind tendency due to vertical EP flux divergence—that is, the vertical wave forcing of the ICON-QBO—and the TEM residuum, we compute their sum to obtain an *effective vertical wave forcing* (Figure 3g). The magnitude of the effective vertical wave forcing looks much more reasonable compared to the remaining TEM zonal wind tendencies than the actual vertical wave forcing. The effective vertical wave forcing also acts to drive a downward propagation of the shear zones of the ICON-QBO, indicating that the actual vertical wave forcing slightly overcompensates for the residuum.

### 4.2. Comparison With the TEM Momentum Budget of the ERA5-QBO

According to the standard QBO paradigm, a lack of downward propagation of the QBO jets can have two possible root causes: a too strong tropical upwelling as part of a too strong Brewer-Dobson circulation (BDC), or a too weak vertical wave forcing, that is, in our case too weak effective vertical wave forcing. In the following, we will investigate which of these two root causes is responsible for the lack of downward propagation of the ICON-QBO by comparing its TEM momentum budget with that of the ERA5-QBO.

For the comparison of QBO momentum budgets, it is essential that they are calculated for the same phase of the QBO. This is usually achieved by constructing so-called QBO composites, which are averages over several QBO cycles referenced at a fixed altitude based on a certain criterion (see, e.g., Bushell et al., 2020; Krismer & Giorgetta, 2014). However, due to the comparatively short simulation period of the ICON simulation, this methodology is not applicable for us. Instead, we compare the momentum budgets of the ICON-QBO and the ERA5-QBO for a fixed period, which is already well away from the initialization of the ICON simulation, but during which both QBOs are still reasonably close to each other. For this purpose, we choose the period 17 May 2004–7 October 2004, which is highlighted by the vertical dashed lines in Figure 1. By doing the comparison for a fixed period, we also ensure that both, the ICON-QBO and the ERA5-QBO have the same seasonal boundary conditions.

Figure 4 shows the TEM momentum budgets of the ICON-QBO and the ERA5-QBO averaged over the analysis period 17 May 2004–7 October 2004 as a function of altitude. Figure 5 shows the accumulated TEM tendencies in the upper (29–34 km) and lower (18–23 km) shear zones of the ICON-QBO and the ERA5-QBO. Both figures indicate that a too strong tropical upwelling is not the root cause for the lack of downward propagation of the ICON-QBO. Throughout the whole QBO domain (17–35 km), the zonal wind tendency due to residual advection, which is dominated by its vertical component, is of comparable magnitude for the ICON-QBO and the ERA5-QBO (Figure 4). Also in both shear zones, the accumulated tendency due to residual advection is in good agreement between the ICON simulation and the ERA5 reanalysis (Figure 5).

This finding is confirmed by Figure 6, which shows the residual vertical velocity $w^*$ averaged over the simulation period. The 30° S–30° N mean $w^*$, a proxy for the strength of the rising branch of the BDC, is weaker in the ICON simulation than in the ERA5 reanalysis at all altitudes, except for two narrow regions around 25 and 34 km. The 5° S–5° N mean $w^*$, which is ultimately relevant for the QBO, is also weaker in ICON than in ERA5 at all

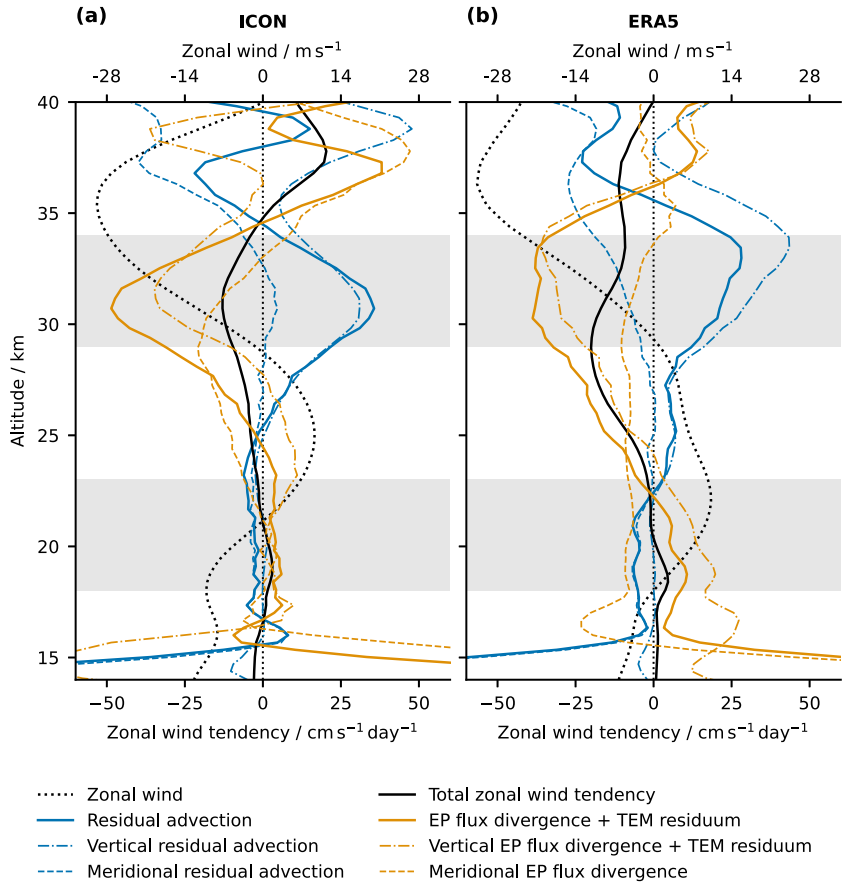


**Figure 4.** 5°S–5°N mean profiles of the transformed Eulerian mean (TEM) zonal wind tendencies averaged over the period 17 May 2004–7 October 2004 in (a) the ICON simulation and in (b) the ERA5 reanalysis. Please note that the residual advection (solid blue curve) is the sum of the vertical residual advection (dashed-dotted blue curve) and the meridional advection (dashed blue curve), and that the EP flux divergence + TEM residuum (solid orange curve) is the sum of the vertical EP flux divergence + TEM residuum (dashed-dotted orange curve) and the meridional EP flux divergence (dashed orange curve). The *x*-axis for the zonal wind $\overline{u}$ is given at the upper spine. Light gray bars mark the altitude ranges of the lower and upper shear zones in Figure 5.

altitudes, except for the altitudes between 24 and 28.5 km. The oscillating vertical structure of the $w^*$ profiles in the ICON simulation, which causes them to locally exceed those of the ERA5 reanalysis, is the imprint of the persistent secondary meridional circulation of the stalling ICON-QBO itself. We conclude that the tropical upwelling associated with the BDC is not too strong in the ICON simulation, but rather too weak compared to the ERA5 reanalysis. Therefore, it cannot be the root cause of the lack of downward propagation of the ICON-QBO.

Before we proceed with the comparison of the wave forcing between the ICON-QBO and the ERA5-QBO, it should be mentioned that it is reasonable to consider the sum of the zonal wind tendency due to the vertical EP flux divergence and the TEM residuum as the effective vertical wave forcing also in the ERA5 reanalysis. In ERA5, the TEM residuum is dominated by the zonal wind tendency of the GW parameterization, so the effective vertical wave forcing represents the total zonal forcing due to vertically propagating waves. So even though the details of the effective vertical wave forcing differ between ICON and ERA5, it is a reasonable measure of the total vertical wave forcing in both cases. Therefore, it is meaningful to compare the effective vertical wave forcing between ICON and ERA5.

In the upper shear zone, the effective vertical wave forcing is in good agreement between the ICON simulation and the ERA5 reanalysis (Figures 5a and 5b). This corresponds well to the overall reasonable downward propagation of this shear zone in the first year of the ICON simulation (Figure 1). In contrast, the effective vertical wave forcing in the lower shear zone is much weaker in the ICON simulation than in the ERA5 reanalysis, and at the end of the analysis period the accumulated effective vertical wave forcing is more than three times weaker in

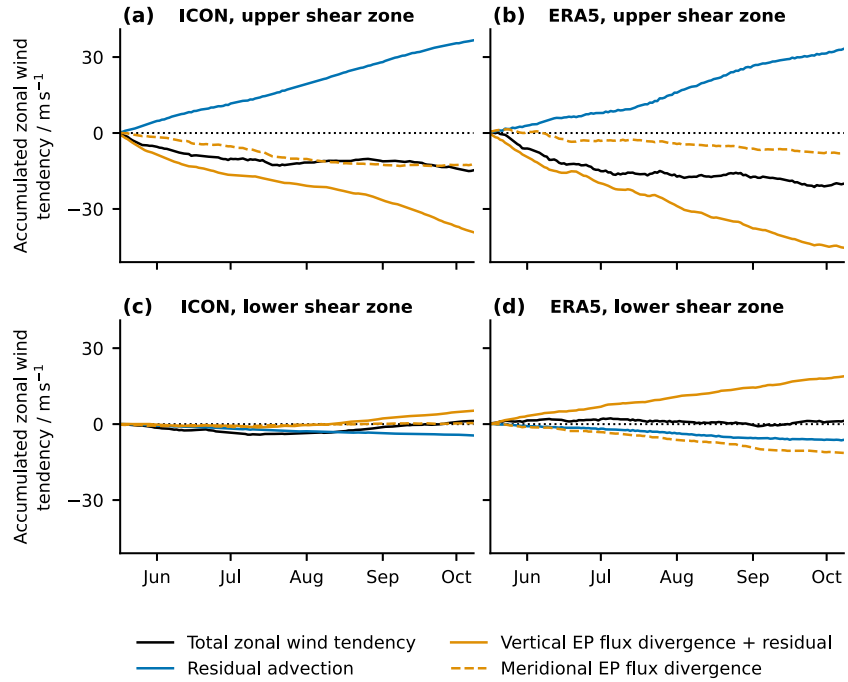


**Figure 5.** Accumulated 5° S–5° N mean transformed Eulerian mean zonal wind tendencies during 17 May 2004–7 October 2004 for (a and c) the ICON simulation and (b and d) the ERA5 reanalysis. Panels (a and b) show tendencies averaged between an altitude of 29 and 34 km, which is representative of the upper QBO shear zone during the accumulation period, and panels (c and d) show tendencies averaged between an altitude of 18 and 23 km, which is representative of the lower QBO shear zone during the accumulation period. These altitude ranges are highlighted in Figure 4.

ICON than in ERA5 (Figures 5c and 5d). This shows that the root cause of the lack of downward propagation of the ICON-QBO in the lowermost stratosphere is a too weak effective vertical wave forcing.

The zonal wind tendency due to meridional EP flux divergence differs qualitatively between the ICON simulation and the ERA5 reanalysis. In ERA5, it is approximately constant throughout the whole QBO domain between 18 and 34 km (Figure 4b), while in ICON it clearly depends on altitude and shows a local maximum in the upper shear zone at ∼30 km (Figure 4a). As a consequence, the accumulated zonal wind tendency due to meridional EP flux divergence in the upper shear zone is twice as large in ICON as in ERA5 at the end of the analysis period (Figures 5a and 5b). This shows that the meridional wave forcing is obviously important for the ICON-QBO and contributes significantly to the downward propagation of the upper shear zone.

Overall, we conclude that the TEM momentum balance of the ICON-QBO in the upper QBO domain during the analysis period is reasonable. Here, the residual advection, the effective vertical wave forcing, and the total zonal wind tendency show good quantitative agreement with ERA5 (Figures 5a and 5b). In contrast, the wave forcing of the ICON-QBO in the lowermost stratosphere is essentially zero and thus substantially weaker than in ERA5, leading to a biased QBO momentum balance. The root cause of the lack of downwelling of the ICON-QBO is a lack of effective vertical wave forcing in the lowermost stratosphere.

### 4.3. Spectral Decomposition of the QBO Wave Forcing

So far, we have only considered the total wave forcing, which does not allow any conclusions to be drawn about the types and scales of the waves driving the ICON-QBO. To understand which parts of the wave spectrum contribute to the wave driving of the ICON simulation and how they compare to the ERA5 reanalysis, we compute zonal wavenumber spectra of the vertical EP flux divergence for the comparison period 17 May 2004–7 October 2004 and average them over the upper (29–34 km) and lower (18–23 km) shear zones of the ICON-QBO and the ERA5-QBO. As shown by Figure 7, small-scale GWs with $k > 100$ contribute substantially to the total vertical EP flux divergence, with a relative contribution of about 75 % in the upper shear zone and about 50 % in the lower

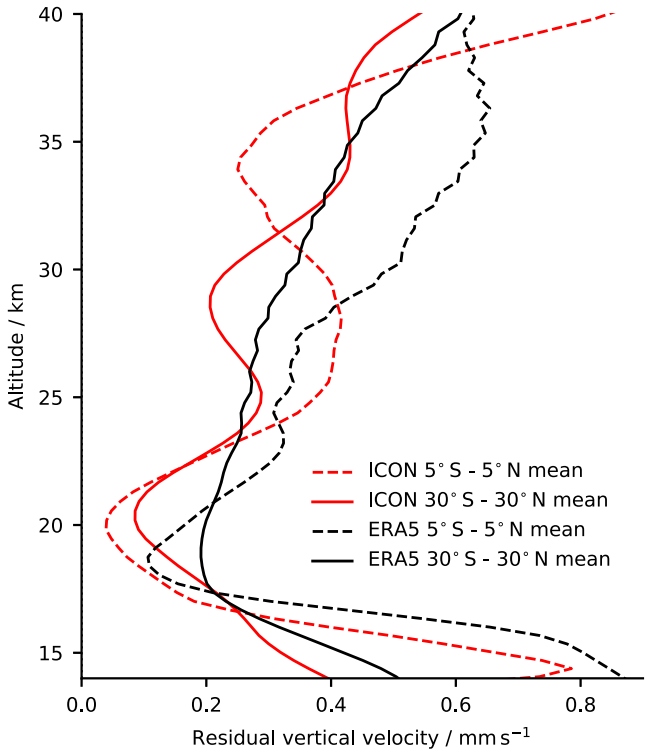


**Figure 6.** Residual vertical velocity $w^*$ of the ICON simulation and the ERA5 reanalysis averaged over the period 1 April 2004–31 March 2006.

shear zone. In contrast, in the ERA5 reanalysis the small-scale GWs with $k > 100$ do no longer contribute to the total vertical EP flux divergence in both shear zones, and already starting at $k = 70$ the resolved vertical EP flux divergence seems to be distorted by the resolution limit, in line with the results of Krismer et al. (2015). Instead, their effect is captured by GW parameterization, which to a first order approximation is represented by the residuum in the TEM momentum budget of the ERA5-QBO. However, it becomes obvious that the absolute zonal wind tendency by the GW parameterization in the ERA5 reanalysis is much lower than the zonal wind tendency due to the vertical EP flux divergence of small-scale GWs with $k > 100$ in the ICON simulation. In addition, Figure 7 shows that the small-scale GWs with $k > 100$ contribute substantially to the overestimation of the total vertical EP flux divergence compared to what would be required to drive the simulated rate of downward propagation of the ICON-QBO, that is, the effective vertical wave forcing, which means that the forcing by small-scale GWs with $k > 100$ is in principle canceled by the TEM residuum. Therefore, we argue that the role that small-scale GWs with $k > 100$ waves play for the biases of the ICON-QBO relative to the ERA5-QBO cannot be reliably assessed, and thus is uncertain.

To understand to what extent waves with $k < 100$ contribute to the lack of vertical wave forcing in the ICON simulation, in particular planetary-scale waves with $k < 18$, we compute zonal wavenumber-frequency spectra of the vertical EP flux and its divergence for 20 non-overlapping, non-tapered 36-day windows spanning the period 11 April 2004–31 March 2006 (see Section 2.3.2 for details). Subsequently, we sum the spectra over certain zonal wavenumber and ground-based zonal phase speed ranges corresponding to different wave types (see Table 1). The time-altitude cross section of the vertical EP flux divergence in the tropical stratosphere associated with these wave types in the ICON simulation and in the ERA5 reanalysis is shown in Figure 8 for eastward propagating waves and in Figure 9 for westward propagating waves. Note that we omit waves with $|k| > 100$ from this analysis because of their uncertain role for the biases of the ICON-QBO as discussed in the previous paragraph. In addition, the zonal wavenumber-frequency spectrum of the vertical EP flux in the ICON simulation suffers from pronounced temporal aliasing at these scales due to the rather coarse output interval of 3 h (see Supporting Information S1).

Figure 8 shows that the absolute magnitude of the zonal wind tendency due to vertical EP flux divergence associated with slow eastward propagating planetary-scale waves, that is, slow equatorial Kelvin waves, in the lower westerly shear zone (i.e., 18–23 km) is much weaker in the ICON simulation than in the ERA5 reanalysis. In the ICON simulation, the wave forcing is further distributed rather uniformly over a wide vertical range (~17–25 km), while in the ERA5 reanalysis it is strongly concentrated in the westerly shear zone in the lowermost stratosphere. These findings suggest that the lack of vertical wave forcing of the ICON-QBO is predominantly due to slow eastward propagating planetary-scale waves. However, the large vertical spread of the vertical wave forcing by those waves in the ICON simulation—and thus the overall weaker eastward wave forcing in the lower westerly shear zone (i.e., 18–23 km) compared to ERA5 (Figures 8g and 8h)—can also be partly attributed to the weak westerly jet of the ICON-QBO itself. The weak westerly jet only allows very slow waves with a ground-based zonal phase speed close to 0 m s$^{-1}$ to dissipate in the shear zone below it, while faster waves can propagate through. Consequently, it is not immediately clear from Figure 8 whether the weak eastward wave forcing in the lower westerly shear zone (i.e., 18–23 km) is the cause or the effect of the weak westerly jet and its lack of downward propagation.

Therefore, we analyze the vertical wave forcing during the first of the 20 windows used for spectral analysis, that is, 11 April 2004–16 May 2004 (Figure 10). During this period, the vertical structure of the ICON-QBO and the magnitude of its jets still agree reasonably well with those of the ERA5-QBO (Figure 1), allowing for a much clearer attribution of cause and effect. As shown in Figure 10b, the total vertical wave forcing by eastward

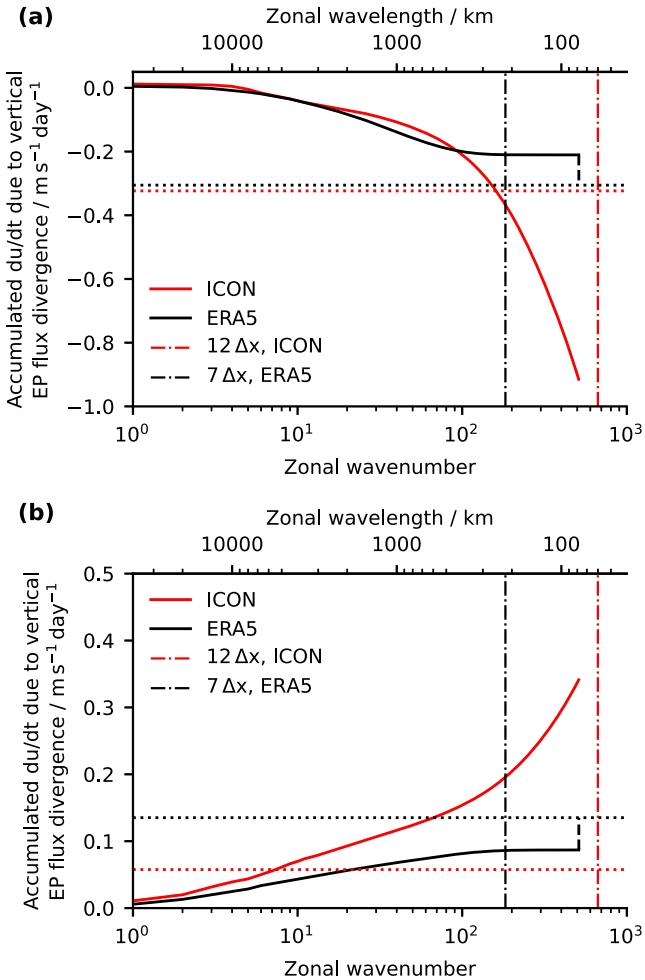


**Figure 7.** 10° S–10° N mean zonal wavenumber spectrum of the cumulative sum of the zonal acceleration due to the divergence of the vertical EP flux averaged over the period 17 May 2004–7 October 2004 and between the altitudes (a) 29 and 34 km and (b) 18 and 23 km. For the ERA5 reanalysis, the dashed vertical line at the end of the spectrum marks the transformed Eulerian mean (TEM) residuum, which is dominated by the contribution of parameterized gravity wave forcing. The horizontal dotted lines mark the effective vertical wave forcing, that is, the vertical wave forcing which would be sufficient to close the TEM momentum budget, while the vertical dashed-dotted lines mark the approximate effective resolutions of ICON and ERA5.

propagating waves with $|k| < 100$ in the lowermost stratosphere is substantially weaker in the ICON simulation than in ERA5, and the majority of this difference is attributable to planetary-scale waves. Therefore, we conclude that lack of downward propagation of the ICON-QBO is mainly due to a lack of vertical wave forcing by slow eastward propagating planetary-scale waves, that is, slow equatorial Kelvin waves.

The vertical wave forcing by eastward propagating intermediate-scale waves behaves very similar to that by slow eastward propagating planetary-scale waves (Figures 8e and 8f). Again, the absolute magnitude of the wave forcing in the lower westerly shear zone (i.e., 18–23 km) is weaker in the ICON simulation than in the ERA5 reanalysis, and it is distributed over a larger vertical range. Obviously, the lack of downward propagation of the ICON-QBO in the lowermost stratosphere is in part also attributable to this wave type. In contrast, the magnitude of the vertical wave forcing of the ICON-QBO by fast eastward propagating planetary-scale waves, that is, fast equatorial Kelvin waves, is overall comparable to that of the ERA5-QBO (Figures 8c and 8d). However, in the ICON simulation a large fraction of this wave forcing also occurs in the easterly shear zone between ∼25 and ∼31 km, and thus opposes the downward propagation of this shear zone. We think that this is likely one reason for the lack of downward propagation of the upper easterly jet of the ICON-QBO in the second year of the simulation.

For westward propagating waves (Figure 9), the differences between the ICON simulation and the ERA5 reanalysis are smaller than for eastward propagating waves. For both the ICON-QBO and the ERA5-QBO, slow westward propagating planetary-scale waves, including $n = 0$ equatorial Rossby waves, do not contribute to the downward propagation of the easterly shear zone, which is initially located between 30 and 38 km (Figures 9a and 9b). In contrast, the downward propagation of this shear zone is mainly driven by fast westward propagating planetary-scale waves, including mixed Rossby-gravity waves (Figures 9c and 9d), and by intermediate-scale westward-propagating waves (Figures 9e and 9f) for both the ICON-QBO and the ERA5-QBO. The vertical wave forcing by these two wave types is in good agreement between the ICON simulation and the ERA5 reanalysis, given the different spatio-temporal structure of their QBOs. This is confirmed by Figure 10a, which also shows reasonable agreement between the vertical wave forcing by westward propagating waves in the ICON simulation and ERA5 during the first of the 20 windows used for spectral analysis, that is, 11 April 2004–16 May 2004.

**Table 1**
*Zonal Wavenumber and Ground-Based Zonal Phase Speed Ranges Corresponding to Different Wave Types for Which We Compute the Vertical EP Flux and Its Divergence*

| Wave type | Zonal wavenumber (eastward) | Zonal wavenumber (westward) | Ground-based zonal phase speed |
|---|---|---|---|
| Slow planetary-scale | $1 \le k \le 18$ | $-18 \le k \le -1$ | $\lvert c\rvert \le 20$ m s$^{-1}$ |
| Fast planetary-scale | $1 \le k \le 18$ | $-18 \le k \le -1$ | $\lvert c\rvert > 20$ m s$^{-1}$ |
| Intermediate-scale | $19 \le k \le 100$ | $-100 \le k \le -19$ | – |

*Note.* Sampling interval of the data of 3 hr does only allow for the detection of waves with a frequency of <4 cpd. Thus, the largest detectable ground-based zonal phase speed of waves with $|k| = 100$ is 18.5 m s$^{-1}$.

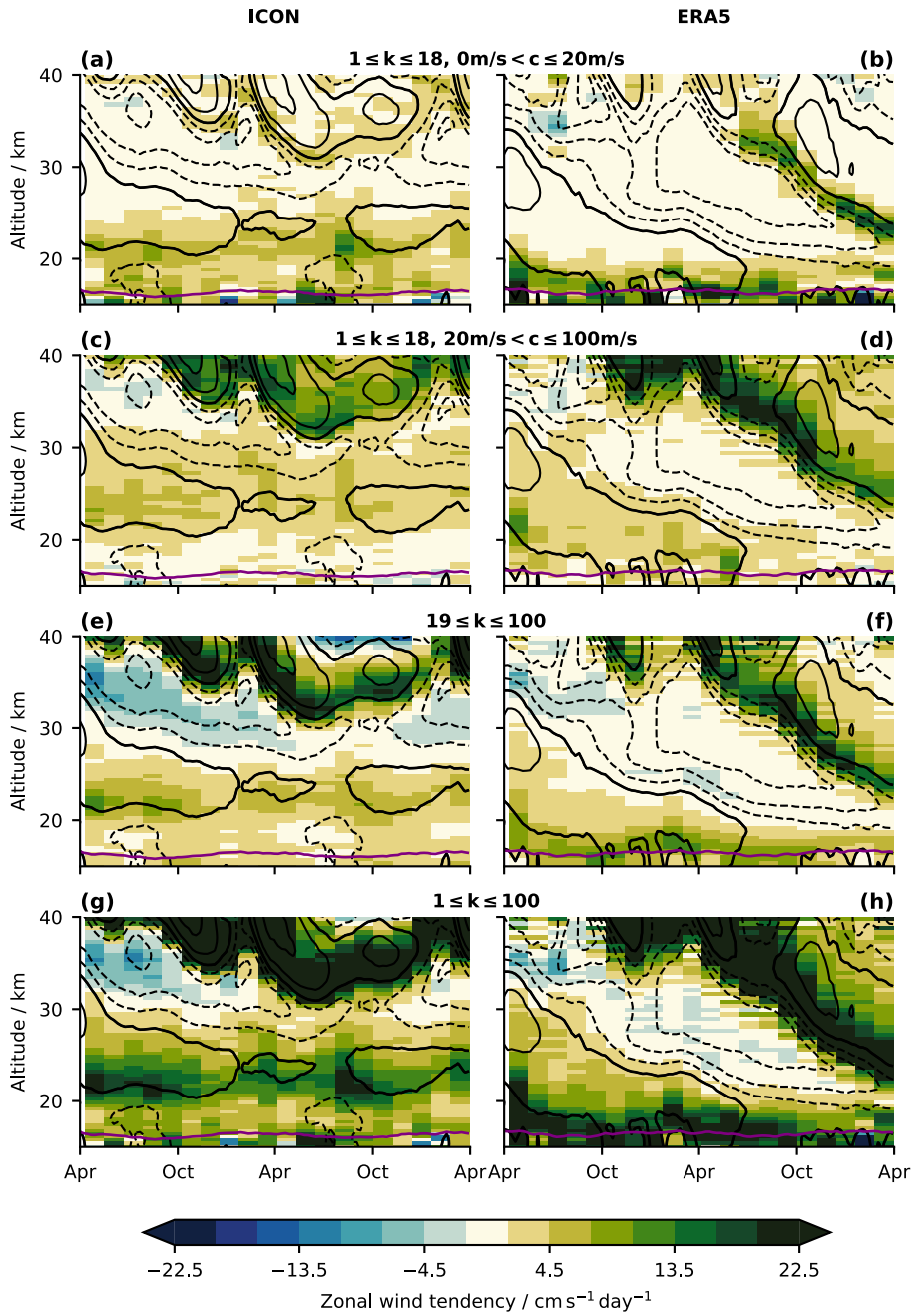


**Figure 8.** Time-altitude cross sections of the 10° S–10° N mean zonal wind tendency due to vertical EP flux divergence associated with eastward propagating waves for (left panels) the ICON simulation and (right panels) the ERA5 reanalysis, separated into different wave types as defined in Table 1: (a and b) slow planetary-scale waves, (c and d) fast planetary-scale waves, (e and f) intermediate-scale waves, (g and h) sum of slow planetary-scale, fast planetary-scale, and intermediate-scale waves. The purple contour lines mark the 370 K-isentrope, which is a proxy for the tropopause altitude.

## 5. Evaluation of the Tropical Wave Field in the ICON Simulation

In the previous section, we showed that the lack of downward propagation of the ICON-QBO in the lowermost stratosphere is due preferably to a lack of vertical wave forcing, that is, a lack of vertical EP flux divergence, associated with eastward propagating planetary-scale waves, mainly comprising equatorial Kelvin waves. In principle, a lack of vertical wave forcing of the QBO can have three possible root causes: (a) a misrepresentation or lack of wave generation in the troposphere, (b) a misrepresentation or lack of vertical wave propagation from

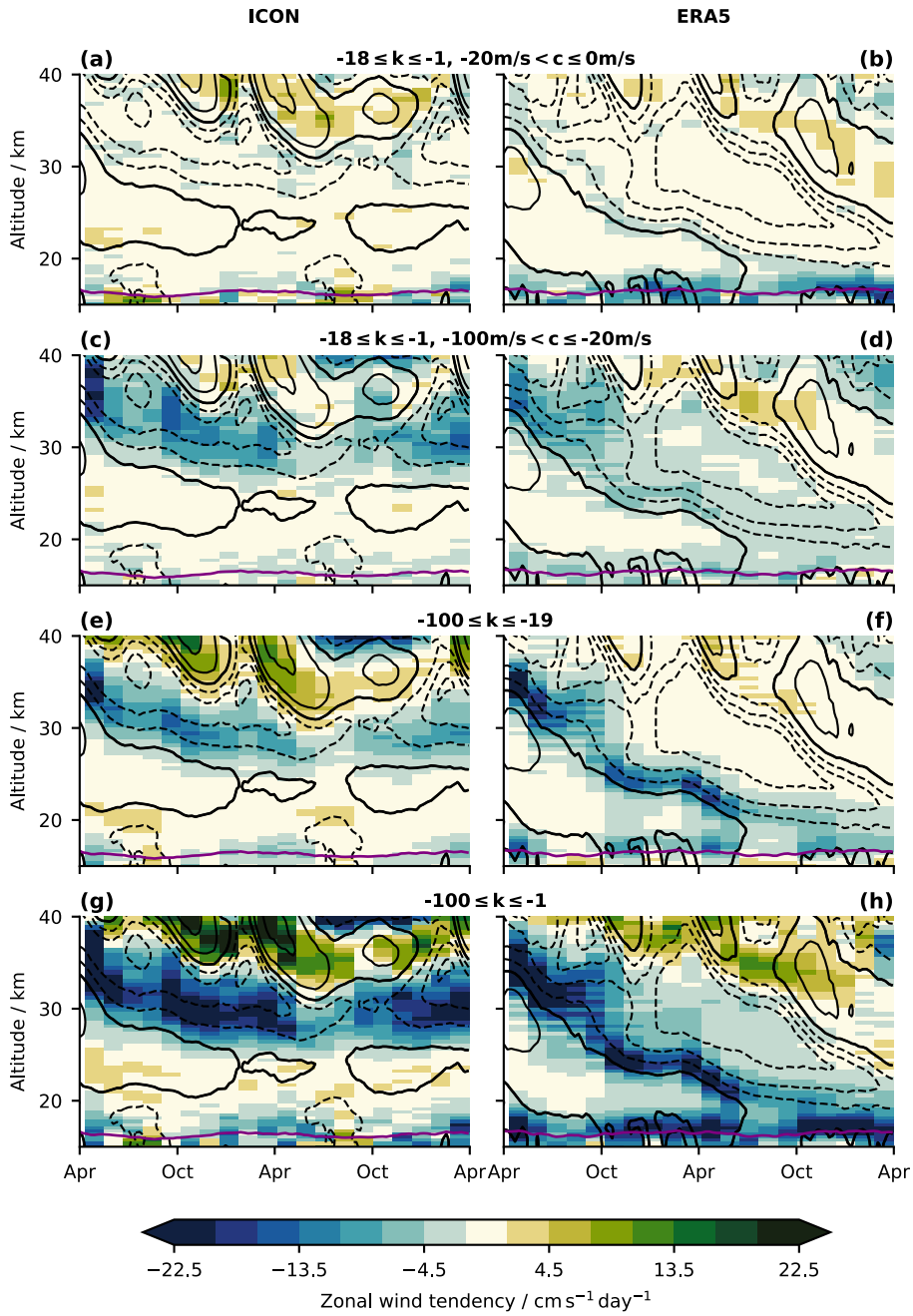


**Figure 9.** As Figure 8, but for westward propagating waves.

the troposphere into the stratosphere, and (c) a misrepresentation or lack of wave dissipation and damping in the shear zones of the QBO. Here, we investigate which of these possible root causes is responsible for the lack of vertical wave forcing in the ICON simulation.

### 5.1. Dissipation and Damping of SEWs in the Lowermost Stratosphere

To analyze the damping and dissipation of SEWs in the ICON simulation, we follow the methodology of Krismer and Giorgetta (2014, see their Section 5c), and consider four different processes: the damping and diffusion of wave-induced zonal wind perturbations by (a) divergence damping, (b) explicit horizontal diffusion, and (c) parameterized vertical diffusion, as well as (d) the damping of wave-induced temperature perturbations by longwave radiation. First, we compute the amplitude spectra of the tendency variables associated with these four

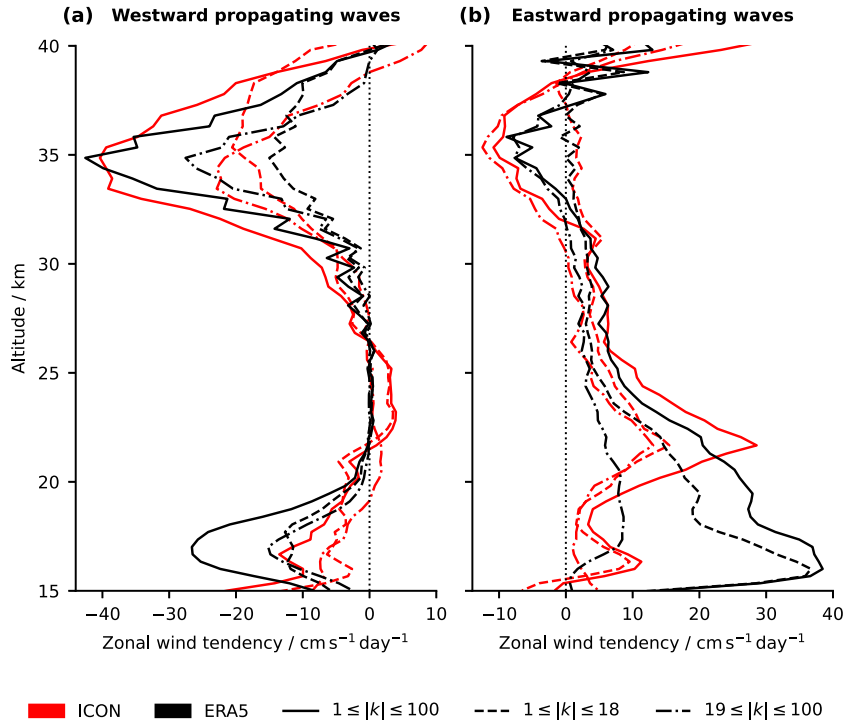


**Figure 10.** Profiles of the 10° S–10° N mean zonal wind tendency due to the vertical EP flux divergence associated with (a) westward propagating waves and (b) eastward propagating waves of different zonal wavenumber ranges in the period 11 April 2004–16 May 2004. The vertical black dotted line marks a zonal wind tendency of 0 m s$^{-1}$ day$^{-1}$.

processes and the corresponding state variable on which the tendency variable acts, as a function of zonal wavenumber and frequency. The spectra are computed for four non-overlapping and non-tapered 36-day windows spanning the period 17 May 2004–7 October 2004, which is the same period we used to compare the zonal momentum budgets of the ICON-QBO and the ERA5-QBO (see Section 4.2). We then average the spectra over all windows and over the 10° S–10° N region. Since we are interested in the damping and dissipation of SEWs in the lower shear zone of the ICON-QBO, we further average the spectra over the 18–23 km altitude range (cf., Section 4.2). The spectra averaged in this way are shown in the left column panels of Figure 11. The right column panels of Figure 11 show the spectra of the quotient of the tendency variable and its corresponding state variable, which can be interpreted as the *e*-folding time of the particular dissipation or damping process associated with the tendency (see Krismer & Giorgetta, 2014). The shorter the *e*-folding time, the more efficient a particular dissipation or damping process is. In the following, we will analyze the dissipation and damping of large-scale waves, as they have been shown to be the main cause of the underestimation of the vertical wave forcing of the ICON-QBO.

The divergence damping appears to strongly damp very slow waves with $\omega < 0.5$ cpd and $|k| > 10$, while only leaving large-scale planetary waves with $|k| < 10$ and $\omega < 0.5$ cpd nearly unaffected (Figure 11b). This is due to the fact that the divergence damping of the zonal wind depends strongly on frequency, but is more or less independent of zonal wavenumber (Figure 11a). It is strongest for very slow or steady perturbations and decreases rapidly with increasing frequency. In principle, this behavior is to be expected because the divergence damping is employed in ICON to remove quasi-stationary small-scale checkerboard patterns. The spectrum of the parameterized vertical diffusion of the zonal wind also shows a first-order dependence on frequency, but it has a larger magnitude than the divergence damping, except for the lowest frequencies (Figure 11c). As a result, parameterized vertical diffusion very efficiently damps all waves except large-scale planetary waves with $|k| < 10$ and $\omega < 0.5$ cpd (Figure 11d). It further is the dominant damping mechanism for waves with $|k| > 15$ across the four mechanisms considered. The explicit horizontal diffusion of the zonal wind is virtually independent of frequency and zonal wavenumber and has a much smaller magnitude than the parameterized vertical diffusion and divergence damping over the entire spectral range considered (Figure 11e). Therefore, explicit horizontal diffusion does not

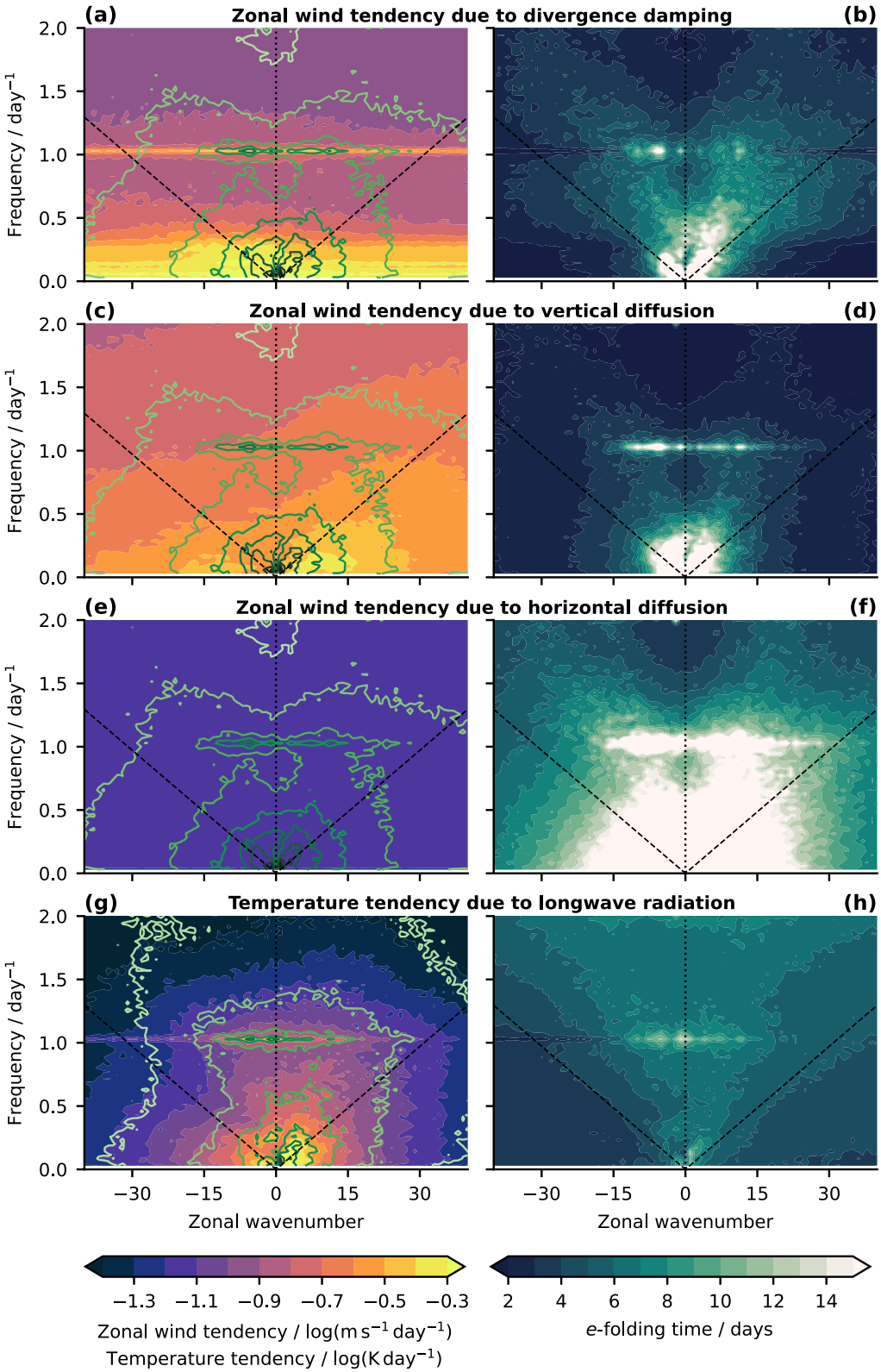


**Figure 11.**

substantially damp waves with $|k| < 25$ and $\omega < 1$ cpd (Figure 11f). For waves with larger zonal wavenumbers and higher frequencies, wave damping by horizontal diffusion is still of secondary importance compared to wave damping by divergence damping and vertical diffusion. In contrast to the diffusive wave damping processes of the zonal wind, the radiative damping of waves depends mainly on intrinsic zonal phase speed and is most efficient for slow waves (Figure 11h), which agrees with theory (e.g., Fels, 1982). Therefore, radiative damping is the dominant damping mechanism of large-scale planetary waves with $|k| < 10$ and $\omega < 0.5$ cpd.

The basic result that planetary-scale waves with $|k| < 10$ and $\omega < 0.5$ cpd are mainly damped by radiation in the ICON simulation, while smaller-scale waves with $|k| > 10$ and higher-frequency waves with $\omega > 0.5$ cpd are mainly damped by diffusive processes, agrees well with the results of Krismer and Giorgetta (2014). The overall damping of large-scale waves in the lower shear zone of the ICON-QBO appears to be reasonable and not distorted. However, we found that the diffusive damping of waves in the ICON simulation is dominated by divergence damping and parameterized vertical diffusion instead of horizontal diffusion. It is unclear to what extent this partitioning of the diffusive wave damping in the ICON simulation is reasonable, and whether it indicates that individual diffusion and damping schemes are too strong or too weak. At least the divergence damping, which is implemented to reduce small-scale checkerboard patterns, has a surprisingly large impact on wave damping.

To validate these conclusions, we analyze the vertical propagation of exemplary Kelvin waves in physical space, which implicitly depends on all possible damping mechanisms present in ICON. Therefore, any gross misrepresentation of wave damping and dissipation in ICON would become apparent in this representation. To isolate the Kelvin waves, we first computed the Fourier transform of the non-tapered but detrended symmetric perturbation temperature in longitude and time. The perturbation temperature is the deviation of the temperature from its zonal and temporal mean. Subsequently, we performed an inverse Fourier transform only on the spectral components with $1 \leq k \leq 10$, $0\,\text{cpd} < \omega \leq 0.4\,\text{cpd}$, and $0\ \text{m s}^{-1} < c \leq 10\ \text{m s}^{-1}$ (very slow Kelvin waves), $10\ \text{m s}^{-1} < c \leq 20\ \text{m s}^{-1}$ (slow Kelvin waves), and $20\ \text{m s}^{-1} < c \leq 50\ \text{m s}^{-1}$ (fast Kelvin waves).

Figure 12 shows the vertical propagation of the equatorial Kelvin waves isolated in this way at a randomly selected equatorial location in the ICON simulation during 17 May 2004–7 October 2004. The spatio-temporal structure of the three different classes of Kelvin waves is reasonable and agrees well with the standard theory of critical level filtering of vertically propagating waves. The filtering of Kelvin waves by the westerly jet of the ICON-QBO, which has a magnitude of 10–20 m s$^{-1}$, clearly depends on their zonal phase speed. The very slow Kelvin waves are more or less completely damped in the lower part of the westerly jet and are absent above it. The slow Kelvin waves are also strongly damped in the westerly shear zone below the westerly jet, but there are still spurious small-amplitude signals of these waves above the westerly jet. The fast Kelvin waves, which do not reach their critical levels within the westerly jet, propagate through the jet without a substantial loss in amplitude. In general, except for the westerly shear zone between 18 and 25 km, there is no substantial damping of the Kelvin waves. Therefore, we conclude that the vertical propagation of equatorial Kelvin waves in the stratosphere and their damping and diffusion are reasonably well represented in the ICON simulation. We rule out a gross misrepresentation of wave damping and propagation as the root cause of the lack of downward propagation of the ICON-QBO, although the diffusion and damping schemes have not been adapted to the employed resolution and thus their more careful calibration may still play out beneficial for the simulation of wave propagation and dissipation.

### 5.2. Vertical EP Flux Spectra in the Lowermost Stratosphere

In the following, we will analyze the vertical EP flux in the ICON simulation at an altitude of 17 km, just above the tropopause, because it allows us to analyze the upward propagating wavefield before it interacts with the QBO

**Figure 11.** 10°S–10°N mean zonal wavenumber-frequency spectra of (left panels) the amplitude of a particular tendency variable (colors) and its corresponding state variable (contours), and of (right panels) the quotient of this particular tendency variable and its corresponding state variable, that is, the *e*-folding time. The spectra were computed for and averaged over four non-overlapping non-tapered 36-day windows during the period 17 May 2004–7 October 2004 They were further averaged between 18 and 23 km, which is representative of the lower shear zone of the ICON-QBO. Contour lines are logarithmic with an interval of (a, c, and e) 0.3 $\log(\text{m s}^{-1})$ and (g) 0.3 $\log(K)$ with darker lines indicating a larger amplitude. Panels (a and b) show the divergence damping of the zonal wind, (c and d) the explicit horizontal diffusion of the zonal wind, (e and f) the parameterized vertical diffusion of the zonal wind, and (g and h) the temperature tendency due to longwave radiation. Black dashed lines in all spectra mark lines of a constant zonal phase speed of $|c| = 15\ \text{ms}^{-1}$ for visual guidance.

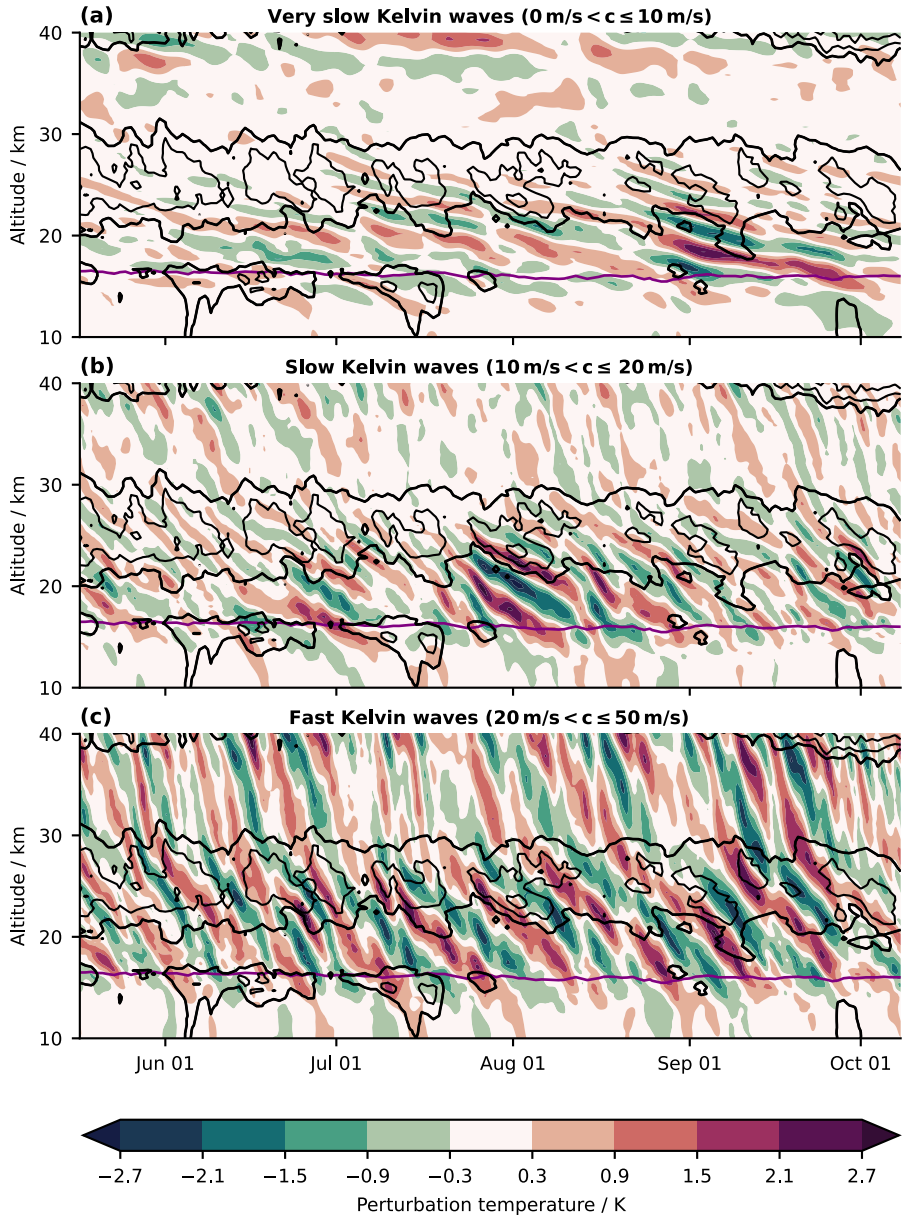


**Figure 12.** Time-altitude cross section of the temperature perturbations induced by (a) very slow Kelvin waves with $0\ \mathrm{m\ s^{-1}} < c \leq 10\ \mathrm{m\ s^{-1}}$, (b) slow Kelvin waves with $10\ \mathrm{m\ s^{-1}} < c \leq 20\ \mathrm{m\ s^{-1}}$, and (c) fast Kelvin waves with $20\ \mathrm{m\ s^{-1}} < c \leq 50\ \mathrm{m\ s^{-1}}$ in the ICON simulation during the period 17 May 2004–7 October 2004 at 0.1756° N, 180° E. Black contour lines show daily mean westerly winds in intervals of $10\ \mathrm{m\ s^{-1}}$, starting at $0\ \mathrm{m\ s^{-1}}$ (thick black contour). Contour lines for easterly winds are not plotted for clarity. The purple contour lines mark the 370 K-isentrope, which is a proxy for the tropopause altitude.

jets. Thus, this analysis can reveal whether the lack of vertical wave forcing of the ICON-QBO is due to an underestimation of the wave momentum fluxes entering the stratosphere. As a first step, we compute the zonal wavenumber-frequency spectra of the vertical EP flux at 17 km for the same 20 non-overlapping, non-tapered 36-day windows spanning the period 11 April 2004–31 March 2006 as in Section 4.3. We then average these spectra over all windows and over the 10°S–10°N region.

Figures 13a and 13b shows the averaged spectra of the vertical EP flux of the ICON simulation and the ERA5 reanalysis. While the basic structure of both spectra agrees, there are notable differences between the ICON simulation and the ERA5 reanalysis. For the ERA5 reanalysis, the spectrum is much smoother than for the ICON

simulation, and it shows some weak organization into a double-lobe structure along phase speeds close to $|c| = 30$ m s$^{-1}$ and $|c| = 50$ m s$^{-1}$. While the spectrum of the ICON simulation organizes along similar phase speed lines, it is substantially noisier than the spectrum of the ERA5 reanalysis. In addition, the spectrum of the ICON simulation is less powerful than that of the ERA5 reanalysis, especially at high frequencies of $\omega > 1$ cpd. At these high frequencies, the vertical EP flux decreases rapidly in the ICON simulation and much faster than in the ERA5 reanalysis.

As shown in Supporting Information S1, the noisy background in the ICON spectrum is the non-physical artifact of a too coarse temporal sampling interval, that is, a too low output frequency. Our output frequency of 3h is insufficient to sample fast and short GWs, which can have periods as short as 10min. This leads to aliasing, which introduces substantial white noise to the spectrum of the vertical EP flux in the ICON simulation (cf., Kirchner, 2005). The spectral noise inhibits a meaningful interpretation of the ICON spectrum for $|k| > 100$.

We further accumulate the averaged zonal wavenumber-frequency spectra of the vertical EP flux over all frequencies. The resulting zonal wavenumber spectra of the vertical EP flux of the ICON simulation and the ERA5 reanalysis are shown in Figure 13c. The spectra reveal that the vertical EP flux associated with small-scale GWs, that is, waves with $|k| > 70$, is much larger for ICON than for ERA5 (Figure 13c). This is explained by the much higher native resolution of the ICON simulation, which allows to resolve a substantially larger fraction of the GW spectrum than ERA5. As shown in Figure S3 in Supporting Information S1, it is explicitly not due to the previously discussed effect of temporal aliasing (cf., Figure S3 in Supporting Information S1). Therefore, it seems that the resolved small-scale GWs with $|k| > 70$ in the ICON simulation take over the role of the parameterized GW forcing in the ERA5 reanalysis and therefore should not be directly compared with the resolved small-scale GWs with $|k| > 70$ in the ERA5 reanalysis. In contrast to small-scale GWs, for both westward and eastward propagating waves with $|k| < 70$, the vertical EP flux is substantially weaker in the ICON simulation than in the ERA5 reanalysis. For eastward propagating waves ($k > 0$), the vertical EP flux in the ICON simulation is about 20% weaker than in the ERA5 reanalysis, approximately uniformly over all zonal wavenumbers up to $k = 70$. For westward propagating waves ($k < 0$), the difference between the ICON simulation and the ERA5 reanalysis is even stronger, and the vertical EP flux in ICON is more than 40% weaker than in ERA5 for zonal wavenumbers between $k = -20$ and $k = -45$.

As the absolute magnitude of the vertical EP flux is generally much larger for planetary-scale waves ($|k| \lesssim 18$) than for smaller-scale waves (see Figure 13c), the uniform relative underestimation of the vertical EP flux in the ICON simulation over a wide range of zonal wavenumbers means that—in absolute terms—the lack of incoming vertical EP flux is largest for planetary-scale waves, which is confirmed by Figure 13d. Therefore, the lack of—mainly planetary-scale—vertical wave forcing of the ICON-QBO (see Section 4.3) can ultimately be attributed to a lack of—mainly planetary-scale—vertical EP flux entering the lower stratosphere.

The fact that the underestimation of the vertical EP flux in the ICON simulation is even more pronounced for westward than for eastward propagating waves can be attributed to differences in upper-tropospheric wave filtering between ICON and ERA5. The ICON simulation has a substantial easterly bias in the upper troposphere and the tropopause region of up to $-6$ m s$^{-1}$ compared to the ERA5 reanalysis (see Figure 14). These easterlies in the ICON simulation result in a strong filtering of slow westward propagating waves, which thus do not reach the lower stratosphere. The strong filtering of slow westward propagating waves in the ICON simulation can be seen in the zonal wavenumber-frequency spectrum of the vertical EP flux, which shows basically no westward, that is, positive, vertical EP flux for westward propagating waves with $-15$ m s$^{-1} < c < 0$ m s$^{-1}$ (Figure 13a, also cf., Figure 13b). This substantial lack of westward EP flux associated with slow westward propagating waves likely contributes to the lack of downward propagation of the easterly shear zone of the ICON-QBO in the second year of the simulation (Figure 1a). Here, the easterly jet becomes so weak that it can only effectively absorb westward propagating waves with $-15$ m s$^{-1} < c < 0$ m s$^{-1}$, which are mostly already filtered out in the upper troposphere. This leaves the easterly jet of the ICON-QBO with virtually no wave forcing.

### 5.3. Spectral Variability of Tropical Precipitation and CCEWs

Most of the upward propagating tropical waves that drive the QBO are generated by latent heat release in deep tropical convection (Fritts & Alexander, 2003; Holton, 1972; Horinouchi et al., 2003; Ricciardulli & Garcia, 2000; Salby & Garcia, 1987). Therefore, the underestimation of the vertical EP flux entering the lowermost

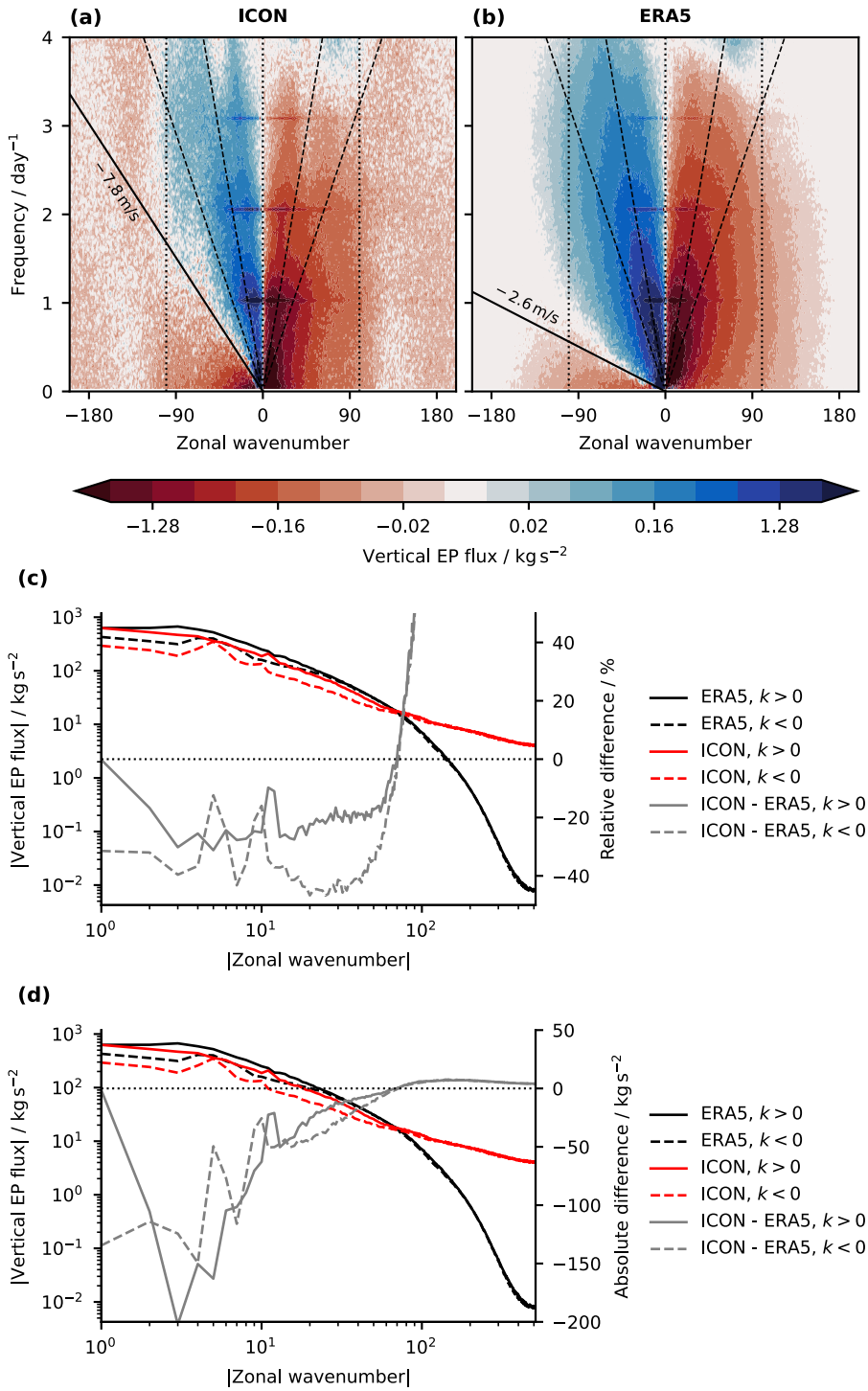


**Figure 13.** Spectral characterization of the 10° S–10° N mean vertical EP flux at an altitude of 17 km, averaged over individual spectra calculated for 20 non-overlapping, non-tapered 36-day windows spanning the period 11 April 2004–31 March 2006. Panels (a and b) show zonal wavenumber-frequency spectra for (a) the ICON simulation and (b) the ERA5 reanalysis. The solid black lines in panels (a and b) mark the zonal mean zonal wind at 17 km of the ICON simulation and the ERA5 reanalysis, respectively, while the dashed black lines mark lines of constant ground-based zonal phase speed of $|c| = 15$ m s$^{-1}$ and $|c| = 30$ m s$^{-1}$. The vertical dotted lines mark the zonal wavenumbers $|k| = 100$ and $k = 0$. Panels (c and d) show the zonal wavenumber spectra of the vertical EP flux in the ICON simulation and in ERA5, with panels (c) and (d) showing the relative and absolute difference between ICON and ERA5, respectively. In panels (c and d), the $y$-axis for the difference between ICON and ERA5 (gray curves) is given at the right spine, and the horizontal dotted line marks a relative and absolute difference of 0% and 0 kg s$^{-2}$, respectively.

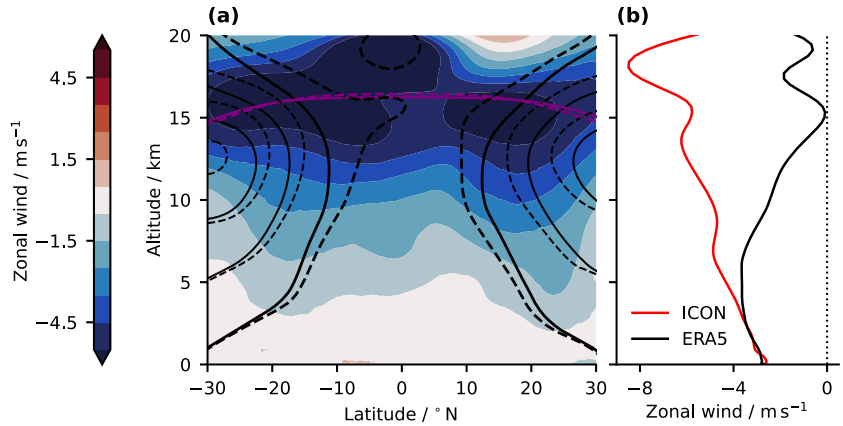


**Figure 14.** (a) Latitude-altitude cross section of the zonal mean zonal wind difference between the ICON simulation and the ERA5 reanalysis, averaged over the period 1 April 2004–31 March 2006. Solid and dashed black contours indicate the zonal mean zonal wind in intervals of 10 m s$^{-1}$ starting at 0 m s$^{-1}$ (bold contours) of the ICON simulation and the ERA5 reanalysis, respectively. Solid and dashed purple contours mark the 370*K*-isentrope, which is a proxy for the tropopause altitude, for the ICON simulation and the ERA5 reanalysis, respectively. (b) 10° S–10° N mean zonal wind in the ICON simulation and the ERA5 reanalysis as a function of altitude.

tropical stratosphere, especially on planetary scales, indicates that wave generation in the tropical troposphere is likely underestimated in the ICON simulation. To investigate the wave sources in the ICON simulation in more detail, we will analyze the spectral variability of tropical precipitation, which is a widely used proxy for latent heating by tropical deep convection. Therefore, we computed zonal wavenumber-frequency spectra of precipitation for the ICON simulation, the ERA5 reanalysis, and the observational precipitation data set IMERG, for 29 tapered 92-day windows with a 34-day overlap spanning the entire simulation period from 01 April 2004–31 March 2006. We then averaged these spectra over all 29 windows and between 15°S and 15°N, and the averaged spectra are shown in Figures 15a–15c.

Figures 15a–15c shows that the ICON simulation reproduces the basic qualitative aspects of the observed tropical precipitation spectrum reasonably well. The spectra of ICON, IMERG, and ERA5 are all red in zonal wavenumber and frequency, but the spectrum of the ICON simulation is slightly smoother than those of IMERG and ERA5. The ICON simulation also shows a clear preference for westward propagating tropical waves, in agreement with IMERG and ERA5. The spectra of the ICON simulation and IMERG both organize along the same lines of constant zonal phase speed, that is, $|c| = 15$ m s$^{-1}$, while the spectrum of ERA5 organizes along lines of constant absolute phase speed of slightly more than 15 m s$^{-1}$.

Quantitatively, however, the precipitation spectra differ substantially between the ICON simulation on the one hand and IMERG and ERA5 on the other. The ICON simulation substantially underestimates the tropical precipitation variance compared to IMERG, over a wide spectral range of about $|k| < 130$ and $\omega < 2$ cpd (see white dashed lines in Figures 15a and 15b). Only for larger wavenumbers and frequencies, the ICON simulation has a slightly larger precipitation variance than IMERG, probably due to its higher native spatial and temporal resolution compared to the IMERG data. Compared to the ERA5 reanalysis, the ICON simulation has a larger tropical precipitation variance in most parts of the spectrum, except for the planetary-scale part, that is, $|k| \leq 18$ and $\omega < 0.5$ cpd, where the tropical precipitation variance is still underestimated in ICON. The fact that the ICON simulation has a larger precipitation variance than the ERA5 reanalysis, except for the planetary-scale part of the spectrum, is due to the fact that ICON explicitly simulates deep convection, while ERA5 parameterizes it. The parameterization of deep convection has been shown to lead to an underestimation of high-frequency precipitation variance compared to observations (e.g., J.-E. Kim & Alexander, 2013). The underestimation of planetary-scale precipitation variance in the ICON simulation compared to the ERA5 reanalysis is also not surprising, since planetary-scale precipitation features in ERA5—although precipitation is a pure model product—are still well constrained by observations and thus, by definition, close to IMERG.

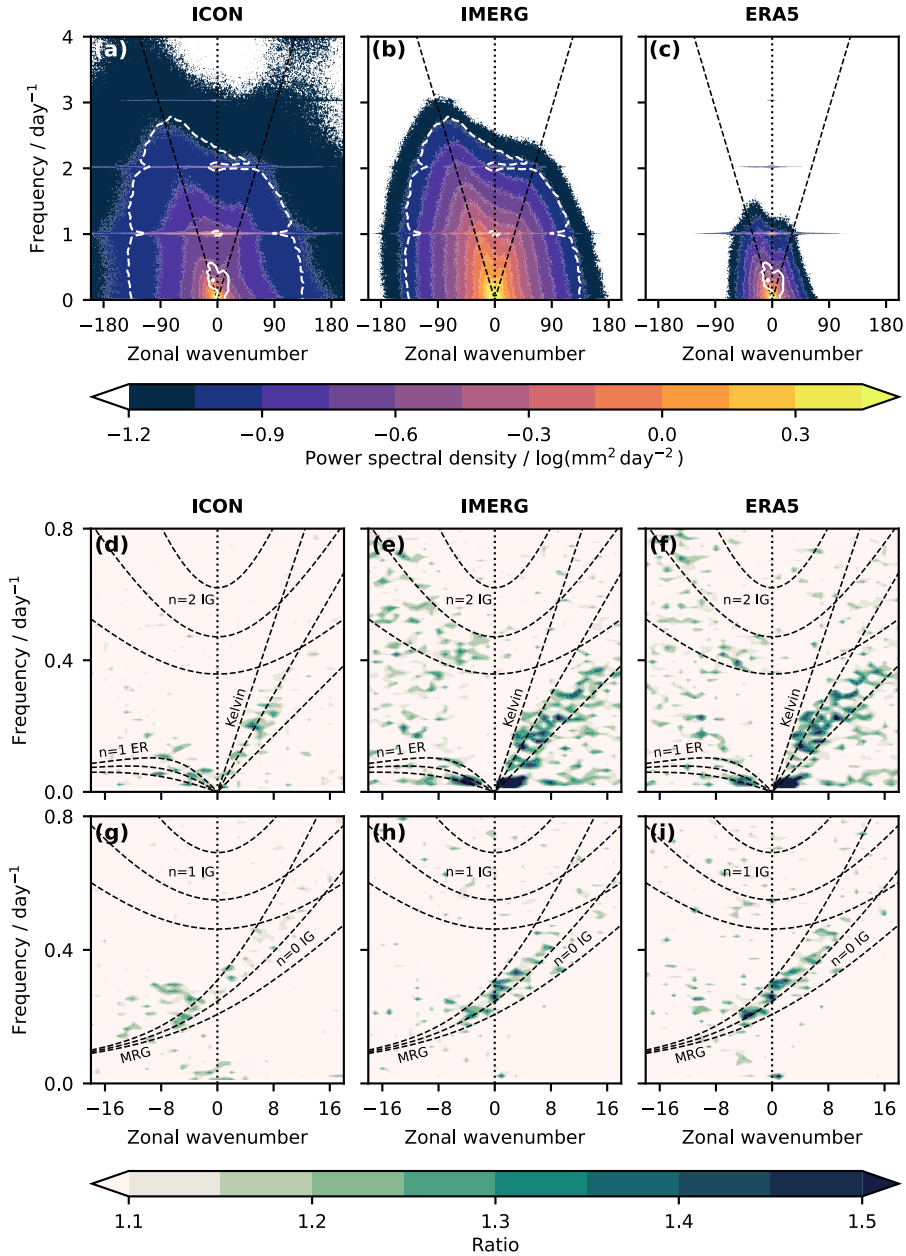


**Figure 15.** 15°S–15°N mean zonal wavenumber-frequency spectra of precipitation variance for (a) the ICON simulation, (b) the observational data set IMERG, and (c) the ERA5 reanalysis, averaged over 29 tapered 92-day windows with a 34-day overlap. White lines in panels (a—c) indicate isolines where the smoothed power spectral density of ICON agrees with (dashed) IMERG and (solid) ERA5. Black dashed lines in panels (a–c) mark a constant ground-based zonal phase speed of $c = 15$ m s$^{-1}$. Panels (d–f) and (g–i) show the 15° S–15° N mean zonal wavenumber-frequency spectra of normalized symmetric and antisymmetric precipitation variance, respectively, for (d and g) the ICON simulation, (e and h) IMERG, and (f and i) ERA5, averaged over 29 92-day windows with a 34-day overlap. The normalization has been performed according to Wheeler and Kiladis (1999). Black dashed lines in (d–i) mark ground-based theoretical dispersion curves of selected convectively coupled equatorial waves with an equivalent depth $h_e$ of 10 m, 30 m, and 90 m. Please note the following abbreviations: ER, Equatorial Rossby wave; IG, Inertia-gravity wave; and MRG, Mixed Rossby-gravity wave.

In general, planetary-scale precipitation variance in the tropics is dominated by CCEWs, which we will analyze in the following using the methodology of Wheeler and Kiladis (1999). Therefore, we computed the zonal wavenumber-frequency spectra of the symmetric and antisymmetric components of tropical precipitation (see

Section 2.3.1 for details) for the same 29 tapered 92-day windows with a 34-day overlap that we computed the raw spectra for. Afterward, we normalized the symmetric and antisymmetric spectra by dividing them by a smoothed background spectrum to highlight spectral peaks representing CCEWs. We then averaged these spectra over all 29 windows and between 15°S and 15°N, and the averaged spectra are shown in Figures 15d–15j.

The normalized symmetric and antisymmetric spectra of the observational data set IMERG and the ERA5 reanalysis are nearly identical. This can be explained by the good observational constraint on planetary-scale precipitation in ERA5. Both IMERG and ERA5 have a rich spectrum of symmetric and antisymmetric CCEWs, including equatorial Kelvin waves, long n = 0 equatorial Rossby waves, mixed Rossby-gravity waves, and n = 0 and n = 2 inertia-gravity waves. In contrast, the ICON simulation shows much less organization of precipitation into CCEWs than IMERG and ERA5. The ICON simulation has only weak signals of equatorial Kelvin waves, long n = 0 equatorial Rossby waves, and mixed Rossby-gravity waves. The signals of n = 0 and n = 2 inertia-gravity waves are practically absent, and the ICON simulation also shows no signal of the Madden-Julian oscillation (MJO). The latter is in stark contrast to IMERG and ERA5, where the MJO appears as a distinct spectral peak in the symmetric spectrum at $1 \leq k \leq 3$ and $\omega < 0.05$ cpd.

To conclude, the ICON simulation suffers from a substantial lack of CCEWs in combination with a general underestimation of spectral precipitation variance compared to the observational data set IMERG. CCEWs are usually closely coupled to SEWs (Kawatani et al., 2009; Maury et al., 2013) that ultimately drive the QBO, and more generally, the spectral characteristics of the tropical precipitation variance have been shown to control the wave momentum fluxes in the lower tropical stratosphere (Horinouchi et al., 2003; Ricciardulli & Garcia, 2000). Therefore, we conclude that the substantial underestimation of CCEWs in the ICON simulation is likely the root cause of the lack of planetary-scale vertical wave momentum flux entering the lowermost stratosphere and, ultimately, the lack of downward propagation of the ICON-QBO.

## 6. Discussion

### 6.1. Answers to the Research Questions

By performing a two-year-long simulation with the GSRM ICON with a horizontal resolution of ∼5 km and a vertical resolution between ∼350 m and ∼560 m in the stratosphere, we addressed the following research questions:

1. *Is a state-of-the-art GSRM capable of directly simulating a full cycle of the QBO in a reasonable way? Which aspects of the QBO are well captured and which are not?*
   No, the current configuration of the state-of-the-art GSRM ICON is not yet capable of reasonably simulating a full QBO cycle. However, ICON does maintain a QBO-like zonal wind structure in the tropical stratosphere throughout the whole simulation. This is already a major achievement, given that a westerly—that is, super-rotational—jet at the equator can only be sustained by QBO-like vertical wave forcing, and the ICON configuration employed was not specifically optimized for this purpose. Furthermore, especially during the first year of the simulation, the representation of the ICON-QBO in the upper QBO domain (i.e., between 25 and 35 km) is in good agreement with the ERA5-QBO. Here, both the magnitude of the jets of the ICON-QBO and the rate of downward propagation of the ICON-QBO are reasonably well represented in the ICON simulation. In the lowermost stratosphere (i.e., below 25 km), however, the ICON-QBO suffers from a pronounced lack of downward propagation right from the beginning of the simulation. During the second year of the simulation, the downward propagation of the ICON-QBO stops completely, and the ICON-QBO also suffers from too shallow and too weak jets.
2. *Why does the model simulate the QBO the way it does?*
3. *If the QBO is reasonably simulated, how is it forced in the simulation? Is it reasonable for the right reasons, or is it the product of compensating errors?*
4. *If the QBO is not reasonably simulated, what are the sources of QBO biases? Are QBO biases caused by biases in other aspects of the simulation?*
   The reasonable downward propagation of the ICON-QBO in the upper QBO domain (i.e., between 25 and 35 km) is the product of an overall reasonable QBO momentum budget. Both the total effective QBO wave forcing and the residual advection of zonal momentum have a magnitude comparable to that of the ERA5 reanalysis. This implies that the downward propagation of the ICON-QBO in the upper QBO domain in the first year of the ICON simulation occurs for the right reasons and is not the consequence of compensating

errors. However, the contribution of the meridional wave forcing to the total effective wave forcing is about twice as large in the ICON simulation as in the ERA5 reanalysis. In the lowermost stratosphere (i.e., below 25 km), the lack of downward propagation of the westerly jet of the ICON-QBO is due to a substantial underestimation of the vertical wave momentum flux entering the lower stratosphere, especially at planetary scales. We attribute this underestimation of the wave momentum flux entering the stratosphere to an underestimation of tropical precipitation variability in general and a pronounced lack of CCEWs in particular. The lack of downward propagation of the upper easterly jet of the ICON-QBO in the second year of the simulation may also be due to the filtering of slow westward propagating waves by an upper-tropospheric easterly bias in the ICON simulation. Please note that the role of small-scale GWs, that is, waves with $|k| > 100$, for the biases of the ICON-QBO could not be reliably assessed due to the large residuum in its TEM momentum budget. Therefore, in addition to planetary-scale waves, small-scale GWs may also contribute to the biases of the ICON-QBO.

### 6.2. Direct QBO Simulations in a GSRM: What Have We Learned, Where Do We Stand?

The overall reasonable representation of QBO dynamics in the easterly shear zone of the ICON-QBO between 25 and 35 km during the first year of the simulation is a promising result. Since the downward propagation of the QBO easterly shear zone is mainly driven by GWs (see Anstey et al., 2022, and references therein), we take it as an indirect indication that a horizontal resolution of ∼5 km is sufficient to simulate a tropical GW spectrum that is in principle able to drive a QBO in a model simulation. This conclusion would be consistent with the results of Polichtchouk et al. (2021), who showed that the total resolved tropical GWMF—which ultimately matters for the QBO—is nearly independent of horizontal resolution in simulations with a horizontal grid spacing of $\mathcal{O}$(10 km)–$\mathcal{O}$(1 km). However, our findings do not imply that the horizontal scales of the GWs that force the QBO in such a simulation match those in nature. This is because Polichtchouk et al. (2021) also showed that the partitioning of the tropical GWMF to zonal wavelengths depends on the horizontal resolution, with the GWMF shifting to shorter zonal wavelengths at higher resolutions. In particular, our findings do thus not allow the conclusion that GWs that are not effectively resolved in our model configuration, that is, GWs with horizontal wavelengths less than 60 km (see Stephan et al., 2019), are irrelevant for driving the QBO in reality.

Furthermore, our results suggest that the wave forcing by meridionally propagating waves may be important for the QBO, at least in the upper QBO domain. Here, the meridional wave forcing contributes about ∼25% to the total wave forcing of the ICON-QBO (see Figure 5a). In contrast, the meridional wave forcing contributes only 10 %–15 % to the total wave forcing in the same altitude range in the ERA5 reanalysis. We speculate that the difference between ICON and ERA5 is mainly due to meridionally propagating GWs in the ICON simulation, which are not resolved in the ERA5 reanalysis. This finding would support recent findings of Y.-H. Kim et al. (2024), who suggest that oblique GW propagation plays a crucial role in QBO dynamics based on results from a novel GW parameterization that allows oblique GW propagation (e.g., Bölöni et al., 2021; Y.-H. Kim et al., 2021). Taking into account that most GW parameterizations do not account for meridional GW propagation, this would also imply that the QBO momentum budgets in conventional GCMs employing simple GW parameterizations may be biased toward too strong vertical wave forcing.

The main bias of the ICON-QBO is a substantial lack of downward propagation in the lowermost stratosphere, which is the result of an underestimation of the vertical wave forcing. Our results suggest that this lack of vertical wave forcing occurs mainly on planetary scales, but it should be considered that the relative contribution of small-scale GWs to this lack of vertical wave forcing could not be reliably quantified. The underestimation of the planetary-scale wave forcing itself can be attributed to a pronounced lack of CCEWs in the tropical troposphere. However, the root cause of the lack of CCEWs and, more generally, the misrepresentation of spatio-temporal variability of tropical deep convection across scales is unclear. Takasuka et al. (2024) showed that careful and targeted tuning of the remaining major parameterizations of a GSRM—that is, the parameterizations of cloud microphysics and turbulent mixing—can greatly improve the model's representation of tropical deep convection on a variety of spatio-temporal scales. Therefore, it seems plausible that an analog tuning approach in the present ICON configuration may help to achieve a more realistic representation of the spatio-temporal variability of tropical deep convection, including CCEWs. Such a tuning approach would further facilitate a deeper understanding of the underlying physics of this spatio-temporal variability of tropical deep convection and its biases, but it also carries the risk of over-tuning, which should be avoided. On the other hand, the lack of CCEWs and spatio-temporal variability of tropical convection may be related to the employed horizontal resolution of ∼5 km,

which is in the convective gray zone and thus should be considered "convection-permitting" rather than "convection-resolving" (e.g., Prein et al., 2015). GSRMs operating in the gray zone have been shown to produce convective clusters that are too small and too intense, preventing convective organization into larger and more long-lived organized convective systems (Becker et al., 2021; Crook et al., 2019). We speculate that this may also hinder the formation of CCEWs and the MJO, implying that a GSRM in the gray zone may still be too coarse to explicitly resolve the generation of the full wave spectrum necessary to drive the QBO in the lowermost stratosphere. In this case, it would be necessary to continue to apply some, ideally scale-aware, parameterization of deep convection or to further increase the horizontal resolution to truly convection-resolving scales, that is, $\Delta x < 1$ km (e.g., Prein et al., 2015). Such an increase in horizontal resolution would have the additional benefit that the simulated GW spectrum would also be more realistic (see Polichtchouk et al., 2021), whereas the further application of a parameterization of deep convection would run counter the motivation for explicit QBO simulations, which is precisely to reduce model complexity in order to enable new fundamental process understanding. Furthermore, as shown by Rackow et al. (2024) for the Integrated Forecasting System of the ECMWF, the application of a parameterization of deep convection does not necessarily guarantee the simulation of a realistic QBO in a km-scale model, although their simulated QBO does not stall as in ICON.

At this point, it should also be mentioned that the CCEWs in the ICON simulation are indeed weak, but not extraordinarily weak compared to conventional GCMs, such as those which participated in QBOi (Holt et al., 2020, see their Figure 2). However, unlike the ICON simulation, the QBOi models simulated a reasonable QBO regardless of their weak CCEWs (Bushell et al., 2020). This is because conventional GCMs can compensate for potential biases in their resolved wave forcing via their GW parameterization, a tuning option GSRMs no longer have. This has further implications: first, it suggests that the simulated QBO in conventional GCMs is often the product of compensating errors, and their QBO momentum budget is rather arbitrary. Second, it implies that a realistic representation of the mean state and the variability of the tropical troposphere is crucial for a realistic representation of the QBO in GSRMs, probably even more so than in conventional GCMs.

Interestingly, a lack of downward propagation of the QBO to the tropopause and a too weak QBO amplitude in the lowermost stratosphere is also a common bias in conventional GCMs (Anstey et al., 2022; Bushell et al., 2020; Schenzinger et al., 2017). In these models, the bias is typically attributed to an insufficient vertical resolution, which does not adequately resolve the vertical propagation and wave-mean flow interactions of waves with small vertical wavelengths, especially planetary-scale Kelvin waves (Anstey et al., 2016; Boville & Randel, 1992; Garfinkel et al., 2022; Geller et al., 2016; Giorgetta et al., 2006). The vertical resolution of the ICON configuration employed (i.e., 350–560 m in the stratosphere) is usually considered sufficient in this regard, and indeed the vertical propagation and damping of Kelvin waves is represented reasonably in the ICON simulation (see Figure 12). However, as suggested by Bramberger et al. (2022) based on observational data, eastward-propagating inertia-gravity waves with large horizontal but very short vertical wavelengths (i.e., <1 km) may also contribute substantially to driving the downward propagation of the QBO in the lowermost stratosphere. Their findings support the model results of Skamarock et al. (2019), who showed that resolved flow features in the free atmosphere, especially mesoscale inertia-gravity waves, converge only at vertical grid spacings of $\leq$200 m, with non-convergence being accompanied by spurious flow features and noise. This suggests that the vertical resolution in the ICON configuration employed may still be too coarse to resolve the full QBO wave forcing.

A general limitation of our findings is that they are based on a relatively short simulation, which further is only representative of one specific QBO phase. Some of our results are based on an even shorter analysis period of less than 5 months. While we do not think that this limitations impact our key results, longer simulations are desirable to achieve statistically more robust results.

## 7. Summary and Prospects

In this study, we present the first attempt at a direct simulation of a full QBO cycle in a GSRM, employing neither a parameterization of deep convection nor GWs. This means that, for the first time, the generation, propagation, and dissipation of the entire wave spectrum driving a QBO in a model is resolved explicitly. For the simulation in this study, we used the state-of-the-art GSRM ICON. Although the details of the QBO-like winds simulated in ICON do not agree with the ERA5 reanalysis—as is to be expected for such a first-of-its-kind simulation—the overall results of the simulation are encouraging. The ICON simulation reproduced the basic zonal momentum budget in the QBO easterly shear zone between 25–35 km during the first boreal summer of the simulation with a

high degree of fidelity. This implicitly suggests that a GSRM with a horizontal grid spacing of $\mathcal{O}$(5 km) basically resolves the relevant processes that drive the QBO in this altitude range, in particular its wave-driving by GWs. Furthermore, we were able to attribute the biases in the simulated QBO to biases in the tropical troposphere, namely an underestimation of the spatio-temporal variability of tropical convection, in particular CCEWs, and excessive wave filtering by an upper-tropospheric easterly zonal wind bias. These results suggest that the realistic representation of the tropical troposphere, in particular the spatio-temporal variability of tropical convection across scales, is currently the biggest roadblock of a successful representation of the QBO in GSRMs—at least in the present one. As a possible way to overcome this roadblock we suggest a targeted retuning of the remaining parameterizations of cloud microphysics and vertical diffusion, but this will likely need to be accompanied by a further increase in horizontal resolution. In contrast to wave generation, the propagation and dissipation of the stratospheric wave spectrum relevant for the simulated QBO do not seem to be a major problem in the present model.

Given the current advances in exascale computing, the ICON configuration employed may soon realistically reach a throughput about 1SYPD, putting multi-decadal global storm-resolving simulations of the QBO within reach (Giorgetta et al., 2022, see their Section 6.5). Direct simulations of a full QBO cycle at horizontal grid spacings close to 1 km or vertical grid spacings of ∼100 m throughout the stratosphere also seem computationally plausible (cf., Neumann et al., 2019). Such simulations have great potential to advance our understanding of the QBO and to resolve long-standing problems, such as the inability of conventional GCMs to reproduce the observed connection between the QBO and the MJO (Martin et al., 2021) or the large uncertainty in the possible response of the QBO to global warming (Richter, Butchart, et al., 2020). Our goal of being able to exploit this exciting technological potential with ICON places clear demands on future work. First and foremost, we need to achieve a realistic representation of CCEWs in ICON—this is the necessary groundwork. Afterward, more detailed sensitivity studies of the QBO with respect to the parameter setting of ICON would help to understand the stringent requirements for a reasonable representation of the QBO in a GSRM. Given this roadmap for future work, accompanied by the concurrently growing technological capabilities, we are optimistic that we will soon achieve the first realistic simulation of the QBO in a GSRM.

## Data Availability Statement

The version of the ICON code used to run the simulation analyzed in this study, as well as the boundary fields for the simulation are available at the data repository Edmond (Franke, 2024). Detailed information on the ICON model are provided by DWD (2024). The ERA5 reanalysis data used for the analysis presented in this study was provided by the Copernicus Climate Change Service (C3S) Climate Data Store (CDS) at the DKRZ (Hersbach et al., 2018a, 2018b). A detailed description of ERA5 is given by Hersbach et al. (2020). The IMERG precipitation data used for the analysis presented in this study was supported by the Integrated Climate Data Center (ICDC), the Center for Earth System Research and Sustainability (CEN), and the University of Hamburg (Huffman et al., 2022). All scripts used to process and analyze the model output and the ERA5 and IMERG raw data are available at the data repository Edmond (Franke, 2024).

**Acknowledgments**
We would like to thank Dmitry Alexeev for assistance in porting the linearized Cariolle ozone scheme to GPU architecture, and Carsten Beyer and Claudia Frauen for technical support in running the ICON simulation on the GPU partition of the supercomputer Levante at the German Climate Computing Centre (Deutsches Klimarechenzentrum, DKRZ). We also thank Sebastián Ortega for providing the basic Python libraries for computing the TEM diagnostics and performing the spectral analysis, and Ulrike Niemeier, Hauke Schmidt, and Ulrich Achatz for valuable discussions at different stages of the manuscript. We acknowledge the Integrated Climate Data Center (ICDC), the Center for Earth System Research and Sustainability (CEN), and the University of Hamburg for supporting the IMERG data. We further acknowledge the German Federal Ministry of Education and Research (BMBF) for partial support through the subproject QUBICC of the program *Role of the Middle Atmosphere in Climate (ROMIC-II)* under Grant 01LG1905A. Last but not least, we would like to thank Inna Polichtchouk and one anonymous reviewer whose review and feedback significantly improved the manuscript. Open Access funding enabled and organized by Projekt DEAL.

## References

Achatz, U., Alexander, M. J., Becker, E., Chun, H.-Y., Dörnbrack, A., Holt, L., et al. (2023). Atmospheric gravity waves: Processes and parameterization. *Journal of the Atmospheric Sciences*, *81*(2), 237–262. https://doi.org/10.1175/JAS-D-23-0210.1

Alexander, M. J., Geller, M., McLandress, C., Polavarapu, S., Preusse, P., Sassi, F., et al. (2010). Recent developments in gravity-wave effects in climate models and the global distribution of gravity-wave momentum flux from observations and models. *Quarterly Journal of the Royal Meteorological Society*, *136*(650), 1103–1124. https://doi.org/10.1002/qj.637

Andrews, D. G., & McIntyre, M. E. (1976). Planetary waves in horizontal and vertical shear: The Generalized Eliassen-Palm relation and the mean zonal acceleration. *Journal of the Atmospheric Sciences*, *33*(11), 2031–2048. https://doi.org/10.1175/1520-0469(1976)033⟨2031:PWIHAV⟩2.0.CO;2

Anstey, J. A., Banyard, T. P., Butchart, N., Coy, L., Newman, P. A., Osprey, S., & Wright, C. J. (2021). Prospect of increased disruption to the QBO in a changing climate. *Geophysical Research Letters*, *48*(15), e2021GL093058. https://doi.org/10.1029/2021GL093058

Anstey, J. A., Osprey, S. M., Alexander, J., Baldwin, M. P., Butchart, N., Gray, L., et al. (2022). Impacts, processes and projections of the quasi-biennial oscillation. *Nature Reviews Earth & Environment*, *3*(9), 588–603. https://doi.org/10.1038/s43017-022-00323-7

Anstey, J. A., Scinocca, J. F., & Keller, M. (2016). Simulating the QBO in an atmospheric general circulation model: Sensitivity to resolved and parameterized forcing. *Journal of the Atmospheric Sciences*, *73*(4), 1649–1665. https://doi.org/10.1175/JAS-D-15-0099.1

Baldauf, M., Seifert, A., Förstner, J., Majewski, D., Raschendorfer, M., & Reinhardt, T. (2011). Operational convective-scale numerical weather prediction with the COSMO model: Description and sensitivities. *Monthly Weather Review*, *139*(12), 3887–3905. https://doi.org/10.1175/MWR-D-10-05013.1

Baldwin, M. P., Gray, L. J., Dunkerton, T. J., Hamilton, K., Haynes, P. H., Randel, W. J., et al. (2001). The quasi-biennial oscillation. *Reviews of Geophysics*, *39*(2), 179–229. https://doi.org/10.1029/1999RG000073

Becker, T., Bechtold, P., & Sandu, I. (2021). Characteristics of convective precipitation over tropical Africa in storm-resolving global simulations. *Quarterly Journal of the Royal Meteorological Society*, *147*(741), 4388–4407. https://doi.org/10.1002/qj.4185

Beres, J. H., Alexander, M. J., & Holton, J. R. (2004). A method of specifying the gravity wave spectrum above convection based on latent heating properties and background wind. *Journal of the Atmospheric Sciences*, *61*(3), 324–337. https://doi.org/10.1175/1520-0469(2004)061⟨0324:AMOSTG⟩2.0.CO;2

Bölöni, G., Kim, Y.-H., Borchert, S., & Achatz, U. (2021). Toward transient subgrid-scale gravity wave representation in atmospheric models. Part I: Propagation model including nondissipative wave-mean-flow interactions. *Journal of the Atmospheric Sciences*, *78*(4), 1317–1338. https://doi.org/10.1175/JAS-D-20-0065.1

Boville, B. A., & Randel, W. J. (1992). Equatorial waves in a stratospheric GCM: Effects of vertical resolution. *Journal of the Atmospheric Sciences*, *49*(9), 785–801. https://doi.org/10.1175/1520-0469(1992)049⟨0785:EWIASG⟩2.0.CO;2

Bramberger, M., Alexander, M. J., Davis, S., Podglajen, A., Hertzog, A., Kalnajs, L., et al. (2022). First super-pressure balloon-borne fine-vertical-scale profiles in the upper TTL: Impacts of atmospheric waves on cirrus clouds and the QBO. *Geophysical Research Letters*, *49*(5), e2021GL097596. https://doi.org/10.1029/2021GL097596

Bushell, A. C., Anstey, J. A., Butchart, N., Kawatani, Y., Osprey, S. M., Richter, J. H., et al. (2020). Evaluation of the quasi-biennial oscillation in global climate models for the SPARC QBO-initiative. *Quarterly Journal of the Royal Meteorological Society*, *148*(744), 1459–1489. https://doi.org/10.1002/qj.3765

Bushell, A. C., Butchart, N., Derbyshire, S. H., Jackson, D. R., Shutts, G. J., Vosper, S. B., & Webster, S. (2015). Parameterized gravity wave momentum fluxes from sources related to convection and large-scale precipitation processes in a global atmosphere model. *Journal of the Atmospheric Sciences*, *72*(11), 4349–4371. https://doi.org/10.1175/JAS-D-15-0022.1

Butchart, N., Anstey, J. A., Hamilton, K., Osprey, S., McLandress, C., Bushell, A. C., et al. (2018). Overview of experiment design and comparison of models participating in phase 1 of the SPARC Quasi-Biennial Oscillation initiative (QBOi). *Geoscientific Model Development*, *11*(3), 1009–1032. https://doi.org/10.5194/gmd-11-1009-2018

Cariolle, D., & Teyssèdre, H. (2007). A revised linear ozone photochemistry parameterization for use in transport and general circulation models: Multi-annual simulations. *Atmospheric Chemistry and Physics*, *7*(9), 2183–2196. https://doi.org/10.5194/acp-7-2183-2007

Crook, J., Klein, C., Folwell, S., Taylor, C. M., Parker, D. J., Stratton, R., & Stein, T. (2019). Assessment of the representation of West African storm lifecycles in convection-permitting simulations. *Earth and Space Science*, *6*(5), 818–835. https://doi.org/10.1029/2018EA000491

Doms, G., Förstner, J., Heise, E., Herzog, H.-J., Mironov, D., Raschendorfer, M., et al. (2021). *COSMO-model version 6.00: A description of the nonhydrostatic regional COSMO-model - Part II: Physical parametrizations* (Technical Report). Deutscher Wetterdienst. https://doi.org/10.5676/DWD_PUB/NWV/COSMO-DOC_6.00_II

Durack, P. J., & Taylor, K. E. (2019). PCMDI AMIP SST and sea-ice boundary conditions version 1.1.6 [Dataset]. *Earth System Grid Federation*. https://doi.org/10.22033/ESGF/input4MIPs.12381

DWD. (2024). ICON model. Retrieved from https://www.icon-model.org

Fels, S. B. (1982). A Parameterization of scale-dependent radiative damping rates in the middle atmosphere. *Journal of the Atmospheric Sciences*, *39*(5), 1141–1152. https://doi.org/10.1175/1520-0469(1982)039⟨1141:APOSDR⟩2.0.CO;2

Franke, H. (2024). Towards the direct simulation of the quasi-biennial oscillation in a global storm-resolving model (Version 2) [Dataset]. *Edmond*. https://doi.org/10.17617/3.A4LJEB

Franke, H., Preusse, P., & Giorgetta, M. (2023). Changes of tropical gravity waves and the quasi-biennial oscillation in storm-resolving simulations of idealized global warming. *Quarterly Journal of the Royal Meteorological Society*, *149*(756), 2838–2860. https://doi.org/10.1002/qj.4534

Frierson, D. M. W., Kim, D., Kang, I.-S., Lee, M.-I., & Lin, J. (2011). Structure of AGCM-simulated convectively coupled Kelvin waves and sensitivity to convective parameterization. *Journal of the Atmospheric Sciences*, *68*(1), 26–45. https://doi.org/10.1175/2010JAS3356.1

Fritts, D. C., & Alexander, M. J. (2003). Gravity wave dynamics and effects in the middle atmosphere. *Reviews of Geophysics*, *41*(1), 1003. https://doi.org/10.1029/2001rg000106

Garfinkel, C. I., Gerber, E. P., Shamir, O., Rao, J., Jucker, M., White, I., & Paldor, N. (2022). A QBO cookbook: Sensitivity of the quasi-biennial oscillation to resolution, resolved waves, and parameterized gravity waves. *Journal of Advances in Modeling Earth Systems*, *14*(3), e2021MS002568. https://doi.org/10.1029/2021MS002568

Geller, M. A., Zhou, T., Shindell, D., Ruedy, R., Aleinov, I., Nazarenko, L., et al. (2016). Modeling the QBO—Improvements resulting from higher-model vertical resolution. *Journal of Advances in Modeling Earth Systems*, *8*(3), 1092–1105. https://doi.org/10.1002/2016MS000699

Giorgetta, M. A., Brokopf, R., Crueger, T., Esch, M., Fiedler, S., Helmert, J., et al. (2018). ICON-A, the atmosphere component of the ICON Earth system model: I. Model description. *Journal of Advances in Modeling Earth Systems*, *10*(7), 1613–1637. https://doi.org/10.1029/2017ms001242

Giorgetta, M. A., Manzini, E., Roeckner, E., Esch, M., & Bengtsson, L. (2006). Climatology and forcing of the quasi-biennial oscillation in the MAECHAM5 model. *Journal of Climate*, *19*(16), 3882–3901. https://doi.org/10.1175/JCLI3830.1

Giorgetta, M. A., Sawyer, W., Lapillonne, X., Adamidis, P., Alexeev, D., Clément, V., et al. (2022). The ICON-A model for direct QBO simulations on GPUs (version icon-cscs:baf28a514). *Geoscientific Model Development*, *15*(18), 6985–7016. https://doi.org/10.5194/gmd-15-6985-2022

Hardiman, S. C., Andrews, D. G., White, A. A., Butchart, N., & Edmond, I. (2010). Using different formulations of the transformed Eulerian mean equations and Eliassen–Palm diagnostics in general circulation models. *Journal of the Atmospheric Sciences*, *67*(6), 1983–1995. https://doi.org/10.1175/2010JAS3355.1

Hersbach, H., Bell, B., Berrisford, P., Biavati, G., Horányi, A., Muñoz Sabater, J., et al. (2018a). ERA5 hourly data on pressure levels from 1979 to present [Dataset]. *Copernicus Climate Change Service (C3S) Climate Data Store (CDS)*. https://doi.org/10.24381/cds.bd0915c6

Hersbach, H., Bell, B., Berrisford, P., Biavati, G., Horányi, A., Muñoz Sabater, J., et al. (2018b). ERA5 hourly data on single levels from 1979 to present [Dataset]. *Copernicus Climate Change Service (C3S) Climate Data Store (CDS)*. https://doi.org/10.24381/cds.adbb2d47

Hersbach, H., Bell, B., Berrisford, P., Hirahara, S., Horányi, A., Muñoz-Sabater, J., et al. (2020). The ERA5 global reanalysis. *Quarterly Journal of the Royal Meteorological Society*, *146*(730), 1999–2049. https://doi.org/10.1002/qj.3803

Holt, L. A., Lott, F., Garcia, R. R., Kiladis, G. N., Cheng, Y.-M., Anstey, J. A., et al. (2020). An evaluation of tropical waves and wave forcing of the QBO in the QBOi models. *Quarterly Journal of the Royal Meteorological Society*, *148*(744), 1541–1567. https://doi.org/10.1002/qj.3827

Holton, J. R. (1972). Waves in the equatorial stratosphere generated by tropospheric heat sources. *Journal of the Atmospheric Sciences*, *29*(2), 368–375. https://doi.org/10.1175/1520-0469(1972)029⟨0368:WITESG⟩2.0.CO;2

Horinouchi, T., Pawson, S., Shibata, K., Langematz, U., Manzini, E., Giorgetta, M. A., et al. (2003). Tropical cumulus convection and upward-propagating waves in middle-atmospheric GCMs. *Journal of the Atmospheric Sciences*, *60*(22), 2765–2782. https://doi.org/10.1175/1520-0469(2003)060⟨2765:TCCAUW⟩2.0.CO;2

Huffman, G., Stocker, E., Bolvin, D., Nelkin, E., & Tan, J. (2022). GPM IMERG final precipitation L3 half hourly 0.1 degree × 0.1 degree V06 [Dataset]. *Goddard Earth Sciences Data and Information Services Center (GES DISC)*. https://doi.org/10.5067/GPM/IMERG/3B-HH/06

Kawatani, Y., Takahashi, M., Sato, K., Alexander, S. P., & Tsuda, T. (2009). Global distribution of atmospheric waves in the equatorial upper troposphere and lower stratosphere: AGCM simulation of sources and propagation. *Journal of Geophysical Research*, *114*(D1), D01102. https://doi.org/10.1029/2008JD010374

Kim, J.-E., & Alexander, M. J. (2013). Tropical precipitation variability and convectively coupled equatorial waves on submonthly time scales in reanalyses and TRMM. *Journal of Climate*, *26*(10), 3013–3030. https://doi.org/10.1175/JCLI-D-12-00353.1

Kim, Y.-H., Bölöni, G., Borchert, S., Chun, H.-Y., & Achatz, U. (2021). Toward transient subgrid-scale gravity wave representation in atmospheric models. Part II: Wave intermittency simulated with convective sources. *Journal of the Atmospheric Sciences*, *78*(4), 1339–1357. https://doi.org/10.1175/JAS-D-20-0066.1

Kim, Y.-H., Voelker, G. S., Bölöni, G., Zängl, G., & Achatz, U. (2024). Crucial role of obliquely propagating gravity waves in the quasi-biennial oscillation dynamics. *Atmospheric Chemistry and Physics*, *24*, 3297–3308. https://doi.org/10.5194/acp-24-3297-2024

Kinne, S., O'Donnel, D., Stier, P., Kloster, S., Zhang, K., Schmidt, H., et al. (2013). MAC-v1: A new global aerosol climatology for climate studies. *Journal of Advances in Modeling Earth Systems*, *5*(4), 704–740. https://doi.org/10.1002/jame.20035

Kirchner, J. W. (2005). Aliasing in $1/f^{\alpha}$ noise spectra: Origins, consequences, and remedies. *Physical Review E*, *71*(6), 066110. https://doi.org/10.1103/physreve.71.066110

Klemp, J. B., Dudhia, J., & Hassiotis, A. D. (2008). An upper gravity-wave absorbing layer for NWP applications. *Monthly Weather Review*, *136*(10), 3987–4004. https://doi.org/10.1175/2008MWR2596.1

Krismer, T. R., & Giorgetta, M. A. (2014). Wave forcing of the quasi-biennial oscillation in the Max Planck Institute Earth System Model. *Journal of the Atmospheric Sciences*, *71*(6), 1985–2006. https://doi.org/10.1175/JAS-D-13-0310.1

Krismer, T. R., Giorgetta, M. A., von Storch, J. S., & Fast, I. (2015). The influence of the spectral truncation on the simulation of waves in the tropical stratosphere. *Journal of the Atmospheric Sciences*, *72*(10), 3819–3828. https://doi.org/10.1175/JAS-D-14-0240.1

Lin, J.-L., Lee, M.-I., Kim, D., Kang, I.-S., & Frierson, D. M. W. (2008). The impacts of convective parameterization and moisture triggering on AGCM-simulated convectively coupled equatorial waves. *Journal of Climate*, *21*(5), 883–909. https://doi.org/10.1175/2007JCLI1790.1

Martin, Z., Son, S.-W., Butler, A., Hendon, H., Kim, H., Sobel, A., et al. (2021). The influence of the quasi-biennial oscillation on the Madden–Julian oscillation. *Nature Reviews Earth & Environment*, *2*(7), 477–489. https://doi.org/10.1038/s43017-021-00173-9

Mauritsen, T., Svensson, G., Zilitinkevich, S. S., Esau, I., Enger, L., & Grisogono, B. (2007). A total turbulent energy closure model for neutrally and stably stratified atmospheric boundary layers. *Journal of the Atmospheric Sciences*, *64*(11), 4113–4126. https://doi.org/10.1175/2007JAS2294.1

Maury, P., Lott, F., Guez, L., & Duvel, J.-P. (2013). Tropical variability and stratospheric equatorial waves in the IPSLCM5 model. *Climate Dynamics*, *40*(9–10), 2331–2344. https://doi.org/10.1007/s00382-011-1273-0

Meinshausen, M., Vogel, E., Nauels, A., Lorbacher, K., Meinshausen, N., Etheridge, D. M., et al. (2017). Historical greenhouse gas concentrations for climate modelling (CMIP6). *Geoscientific Model Development*, *10*(5), 2057–2116. https://doi.org/10.5194/gmd-10-2057-2017

Neumann, P., Düben, P., Adamidis, P., Bauer, P., Brück, M., Kornblueh, L., et al. (2019). Assessing the scales in numerical weather and climate predictions: Will exascale be the rescue? *Philosophical Transactions of the Royal Society A: Mathematical, Physical and Engineering Sciences*, *377*(2142), 20180148. https://doi.org/10.1098/rsta.2018.0148

Osprey, S. M., Butchart, N., Knight, J. R., Scaife, A. A., Hamilton, K., Anstey, J. A., et al. (2016). An unexpected disruption of the atmospheric quasi-biennial oscillation. *Science*, *353*(6306), 1424–1427. https://doi.org/10.1126/science.aah4156

Pahlavan, H. A., Fu, Q., Wallace, J. M., & Kiladis, G. N. (2021). Revisiting the quasi-biennial oscillation as seen in ERA5. Part I: Description and momentum budget. *Journal of the Atmospheric Sciences*, *78*(3), 673–691. https://doi.org/10.1175/JAS-D-20-0248.1

Pahlavan, H. A., Wallace, J. M., Fu, Q., & Kiladis, G. N. (2021). Revisiting the quasi-biennial oscillation as seen in ERA5. Part II: Evaluation of waves and wave forcing. *Journal of the Atmospheric Sciences*, *78*(3), 693–707. https://doi.org/10.1175/JAS-D-20-0249.1

Pincus, R., Mlawer, E. J., & Delamere, J. S. (2019). Balancing accuracy, efficiency, and flexibility in radiation calculations for dynamical models. *Journal of Advances in Modeling Earth Systems*, *11*(10), 3074–3089. https://doi.org/10.1029/2019MS001621

Pithan, F., Angevine, W., & Mauritsen, T. (2015). Improving a global model from the boundary layer: Total turbulent energy and the neutral limit Prandtl number. *Journal of Advances in Modeling Earth Systems*, *7*(2), 791–805. https://doi.org/10.1002/2014ms000382

Plougonven, R., de la Cámara, A., Hertzog, A., & Lott, F. (2020). How does knowledge of atmospheric gravity waves guide their parameterizations? *Quarterly Journal of the Royal Meteorological Society*, *146*(728), 1529–1543. https://doi.org/10.1002/qj.3732

Polichtchouk, I., Wedi, N., & Kim, Y.-H. (2021). Resolved gravity waves in the tropical stratosphere: Impact of horizontal resolution and deep convection parametrization. *Quarterly Journal of the Royal Meteorological Society*, *148*(742), 233–251. https://doi.org/10.1002/qj.4202

Prein, A. F., Langhans, W., Fosser, G., Ferrone, A., Ban, N., Goergen, K., et al. (2015). A review on regional convection-permitting climate modeling: Demonstrations, prospects, and challenges. *Reviews of Geophysics*, *53*(2), 323–361. https://doi.org/10.1002/2014RG000475

Rackow, T., Pedruzo-Bagazgoitia, X., Becker, T., Milinski, S., Sandu, I., Aguridan, R., et al. (2024). Multi-year simulations at kilometre scale with the Integrated Forecasting System coupled to FESOM2.5/NEMOv3.4. *EGUsphere*, *2024*, 1–59. https://doi.org/10.5194/egusphere-2024-913

Ricciardulli, L., & Garcia, R. R. (2000). The excitation of equatorial waves by deep convection in the NCAR Community Climate Model (CCM3). *Journal of the Atmospheric Sciences*, *57*(21), 3461–3487. https://doi.org/10.1175/1520-0469(2000)057⟨3461:TEOEWB⟩2.0.CO;2

Richter, J. H., Anstey, J. A., Butchart, N., Kawatani, Y., Meehl, G. A., Osprey, S., & Simpson, I. R. (2020). Progress in simulating the quasi-biennial oscillation in CMIP models. *Journal of Geophysical Research: Atmospheres*, *125*(8), e2019JD032362. https://doi.org/10.1029/2019JD032362

Richter, J. H., Butchart, N., Kawatani, Y., Bushell, A. C., Holt, L., Serva, F., et al. (2020). Response of the quasi-biennial oscillation to a warming climate in global climate models. *Quarterly Journal of the Royal Meteorological Society*, *148*(744), 1490–1518. https://doi.org/10.1002/qj.3749

Richter, J. H., Sassi, F., & Garcia, R. R. (2010). Toward a physically based gravity wave source parameterization in a general circulation model. *Journal of the Atmospheric Sciences*, *67*(1), 136–156. https://doi.org/10.1175/2009JAS3112.1

Salby, M. L., & Garcia, R. R. (1987). Transient response to localized episodic heating in the tropics. Part I: Excitation and short-time near-field behavior. *Journal of the Atmospheric Sciences*, *44*(2), 458–498. https://doi.org/10.1175/1520-0469(1987)044⟨0458:TRTLEH⟩2.0.CO;2

Satoh, M., Stevens, B., Judt, F., Khairoutdinov, M., Lin, S.-J., Putman, W. M., & Düben, P. (2019). Global cloud-resolving models. *Current Climate Change Reports*, *5*(3), 172–184. https://doi.org/10.1007/s40641-019-00131-0

Schenzinger, V., Osprey, S., Gray, L., & Butchart, N. (2017). Defining metrics of the quasi-biennial oscillation in global climate models. *Geoscientific Model Development*, *10*(6), 2157–2168. https://doi.org/10.5194/gmd-10-2157-2017

Schirber, S., Manzini, E., Krismer, T., & Giorgetta, M. (2015). The quasi-biennial oscillation in a warmer climate: Sensitivity to different gravity wave parameterizations. *Climate Dynamics*, *45*(3–4), 825–836. https://doi.org/10.1007/s00382-014-2314-2

Simmons, A., Soci, C., Nicolas, J., Bell, B., Berrisford, P., Dragani, R., et al. (2020). Global stratospheric temperature bias and other stratospheric aspects of ERA5 and ERA5.1. *ECMWF Technical Memoranda* (p. 859). https://doi.org/10.21957/rcxqfmg0

Skamarock, W. C., Snyder, C., Klemp, J. B., & Park, S.-H. (2019). Vertical resolution requirements in atmospheric simulation. *Monthly Weather Review*, *147*(7), 2641–2656. https://doi.org/10.1175/MWR-D-19-0043.1

SPARC. (2022). In M. Fujiwara, G. Manney, L. Gray, & J. Wright (Eds.), *SPARC Reanalysis Intercomparison Project (S-RIP) Final Report*, *SPARC Report No. 10, WCRP-6/2021*. https://doi.org/10.17874/800DEE57D13

Stephan, C. C., Strube, C., Klocke, D., Ern, M., Hoffmann, L., Preusse, P., & Schmidt, H. (2019). Gravity waves in global high-resolution simulations with explicit and parameterized convection. *Journal of Geophysical Research: Atmospheres*, *124*(8), 4446–4459. https://doi.org/10.1029/2018jd030073

Stevens, B., Satoh, M., Auger, L., Biercamp, J., Bretherton, C. S., Chen, X., et al. (2019). DYAMOND: The DYnamics of the Atmospheric general circulation Modeled On Non-hydrostatic Domains. *Progress in Earth and Planetary Science*, *6*(61), 61. https://doi.org/10.1186/s40645-019-0304-z

Straub, K. H., Haertel, P. T., & Kiladis, G. N. (2010). An analysis of convectively coupled Kelvin waves in 20 WCRP CMIP3 global coupled climate models. *Journal of Climate*, *23*(11), 3031–3056. https://doi.org/10.1175/2009JCLI3422.1

Takasuka, D., Kodama, C., Suematsu, T., Ohno, T., Yamada, Y., Seiki, T., et al. (2024). How can we improve the seamless representation of climatological statistics and weather toward reliable global K-scale climate simulations? *Journal of Advances in Modeling Earth Systems*, *16*(2), e2023MS003701. https://doi.org/10.1029/2023MS003701

Tomassini, L., Willett, M., Sellar, A., Lock, A., Walters, D., Whitall, M., et al. (2023). Confronting the convective gray zone in the global configuration of the Met Office Unified Model. *Journal of Advances in Modeling Earth Systems*, *15*(5), e2022MS003418. https://doi.org/10.1029/2022MS003418

Wheeler, M., & Kiladis, G. N. (1999). Convectively coupled equatorial waves: Analysis of clouds and temperature in the wavenumber–frequency domain. *Journal of the Atmospheric Sciences*, *56*(3), 374–399. https://doi.org/10.1175/1520-0469(1999)056⟨0374:CCEWAO⟩2.0.CO;2

Yao, W., & Jablonowski, C. (2013). Spontaneous QBO-like oscillations in an atmospheric model dynamical core. *Geophysical Research Letters*, *40*(14), 3772–3776. https://doi.org/10.1002/grl.50723

Yao, W., & Jablonowski, C. (2015). Idealized quasi-biennial oscillations in an ensemble of dry GCM dynamical cores. *Journal of the Atmospheric Sciences*, *72*(6), 2201–2226. https://doi.org/10.1175/JAS-D-14-0236.1

Zängl, G., Reinert, D., Rípodas, P., & Baldauf, M. (2015). The ICON (ICOsahedral Non-hydrostatic) modelling framework of DWD and MPI-M: Description of the non-hydrostatic dynamical core. *Quarterly Journal of the Royal Meteorological Society*, *141*(687), 563–579. https://doi.org/10.1002/qj.2378